Journal Pre-proof

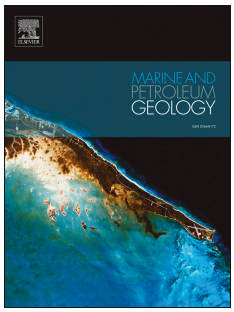

Microstructure and pore systems of shallow-buried fluvial mudstone caprocks in Zhanhua Depression, east China inferred from SEM and MICP

Yuyuan Li, Ming Zha, Rongcai Song, Andrew C. Aplin, Leon Bowen, Xingmou Wang, Yunyin Zhang

PII: S0264-8172(21)00292-0

DOI: https://doi.org/10.1016/j.marpetgeo.2021.105189

Reference: JMPG 105189

To appear in: *Marine and Petroleum Geology*

Received Date: 7 February 2021

Revised Date: 8 June 2021

Accepted Date: 9 June 2021

Please cite this article as: Li, Y., Zha, M., Song, R., Aplin, A.C., Bowen, L., Wang, X., Zhang, Y., Microstructure and pore systems of shallow-buried fluvial mudstone caprocks in Zhanhua Depression, east China inferred from SEM and MICP, *Marine and Petroleum Geology*, https://doi.org/10.1016/j.marpetgeo.2021.105189.

Microstructure and pore systems of shallow-buried fluvial mudstone caprocks in Zhanhua Depression, east China inferred from SEM and MICP

Yuyuan Li[a, b]*, Ming Zha[c], Rongcai Song[b]*, Andrew C. Aplin[d], Leon Bowen[e], Xingmou Wang[f], Yunyin Zhang[f]

[a] Post-Doctoral Research Station of Geological Resource and Geological Engineering, Chengdu University of Technology, Chengdu, Sichuan, 610059, China

[b] College of Energy Resources, Chengdu University of Technology, Chengdu, Sichuan, 610059, China

[c] School of Geosciences, China University of Petroleum, Qingdao, Shandong, 266580, China

[d] Department of Earth Sciences, Durham University, Durham, DH1 3LE, UK

[e] Department of Physics, Durham University, Durham, DH1 3LE, UK

[f] Geophysical Research Institute, Shengli Oilfield Company, SINOPEC, Shandong, 257022, China

*Corresponding author.

E-mail address: yy.li111@foxmail.com (Y. Li) ; songrongcai06@cdut.edu.cn (R. Song)

Abstract

Shallow-buried fluvial mudstones are of great significance as potential top seals for natural gas accumulations in the Zhanhua depression. Four samples were chosen to represent the range of fine-grained microfacies, from clay-rich to silt-rich to cemented, and mercury injection capillary pressure (MICP) porosimetry is combined with Scanning Electron Microscopy (SEM) to characterize microstructure and pore systems quantitatively. The nature of the pore systems that allow capillary breakthrough and thus leakage, were also estimated. Pore areas inferred from SEM data, obtained from representative elementary areas (REAs), follow a similar power law distribution to bulk sample MICP within a specific range, indicating that pores with areas larger than 10^3 nm^2 are well connected. In samples without carbonate cement, pores within the clay matrix are larger in coarser-grained, siltier samples, and there are more pores at the edges of non-clay minerals; this results from force chains of large grains shouldering more effective stress. With increasing silt content, SEM-visible porosity increases and the contribution of pores between non-clay minerals grows significantly, while the contribution of pores within clay matrix reduces. In more clay-rich samples, capillary breakthrough is estimated to occur in pores associated with the clay matrix; in siltier samples, breakthrough will occur at lower entry pressures associated with larger interparticle pores. Carbonate cements play a key role in reducing pore space in some siltier samples by partially filling interparticle pores at (a) the interfaces between clay and non-clay minerals, and (b) pores between non-clay minerals areas larger than 10^6 nm^2. By filling larger pores, capillary breakthrough in carbonate-cemented samples occurs at relative high entry pressures through pores in the clay matrix. However, carbonate cements, generally less than 20%, are not sufficient to enable silt-rich mudstones to become effective barriers. Clay content is the most critical control on mudstone seal capacity.

Keywords

Zhanhua depression; Fluvial mudstone; SEM imaging; Pore size distribution; Capillary breakthrough

1. Introduction

Mudstones, sedimentary rocks with 50% or more silt- and clay-sized material with grain sizes < 62.5 μm (Macquaker and Adams, 2003), control the retention of fluids in sedimentary basins (Aplin and Macquaker, 2011). They are targets as unconventional oil and gas reservoirs (Hu et al., 2019; Meng et al. 2020; Meng et al., 2020) and are bounding formations and caprocks for hydrocarbons, hazardous waste storage (Davy et al., 2009) and the subsurface containment of anthropogenic CO_2 and H_2 (Armitage et al., 2010; Lu et al., 2011).

Some of the general controls on the nature of mudstone pore systems have been explored over many years. Both Yang and Aplin (1998) and Aplin and Moore (2016) demonstrated the important role of grain size distribution as a control on pore size distributions, so that at a given porosity, finer-grained, more clay-rich lithologies have smaller pores. However, the diversity of mudstone lithology and mineralogy, coupled with the possibility of different diagenetic pathways (Armitage et al., 2013; Lu et al., 2011), means that care is needed when extrapolating simple grain size-pore size rules to other geological formations.

The threshold capillary entry pressure that must be overcome to allow bulk flow of a non-wetting fluid into a caprock, depends on three factors: the radius of the largest connected pore throats, wettability and the petroleum-water interfacial tension (Downey, 1984). Controls on the origin and nature and connectivity of mudstone pore systems, especially of the largest pores, are thus critical but are only known in a quite general sense. Pore types, along with their diverse origins, and arrangements have different effects on the sealing capacity (Dewhurst et al., 2002; McCreesh et al., 1991). Matrix-related pores in mudstones, formed by both depositional and diagenetic processes, range from simple to complex in shape and origin (Armitage et al., 2010). In addition, although it is well established that mudstone porosity decreases with increasing effective stress (Aplin et al., 2006), the relative roles of mechanical compaction and diagenesis on pore systems, are still incompletely understood (Klaver et al., 2012).

In recent years, numerous techniques have been used to characterize pore systems, including: SEM , TEM (transmission electron microscopy), gas adsorption, MICP and NMR (nuclear magnetic resonance) (Lai et al., 2018; Lai et al., 2019; Mathia et al., 2019). However, different technologies have their own strengths and limitations. MICP is a quick and widely used technique

(Houben et al., 2014; Klaver et al., 2015), which provides a porosity for connected pores of a given radius or equivalent intrusion pressure according to the Washburn equation (Washburn, 1921). The pore throat size distribution is obtained from the intrusion volumes per pressure step. Gas adsorption (N_2, CO_2, CH_4) is another widely used fluid invasion technique, which gives information on surface area and pore size distribution (Mathia et al., 2019; Zhang et al., 2017). One potential problem is that the information obtained from these techniques are based on simplified models of tube, slit or spherical-shaped pores which are not necessarily appropriate for fine-grained sediments. In addition, results of these techniques have rarely been linked to a detailed description of mineralogy, or texture.

Recent studies have shown that the pore network can be studied at nano-scale resolution using SEM (Desbois et al., 2009; Loucks et al., 2009). The combination of Broad Ion Beam (BIB) for high-quality surface preparation and SEM imaging gives access to the representative areas in shales that can be used to quantify microstructure and pore space. Following the basic principles of stereology (Underwood, 1970), the 2D area fraction in a large representative area is a good estimate of the 3D bulk porosity. Imaging at high magnification also provides insight into pore sizes, morphologies, distribution, and cracks caused by drying, stress, and sample preparation (Klaver et al., 2015).

Shallow-buried mudstones play an essential role in the Jiyang sub-basin, as almost 90% of the proven natural gas reserves occur in shallow Neogene gas pools (Zhu et al., 2005). In addition, the formation is also considered as an excellent candidate for CO_2 sequestration in the Bohai Bay Basin (Pang et al., 2012).The purpose of this investigation is to explore controls of the pore network and sealing capacity of shallow-buried, fluvial mudstones of the Guantao formation in the Jiyang sub-basin, with a special focus on pore characterization in samples with different mineralogical and grain size compositions.

MICP is used to gain insight into the connected pore network to the bulk porosities and transport properties of the samples. Pore size distributions and pore morphologies of the mudstones are described quantitatively using a combination of BIB milling and SEM imaging of REAs. The pore size distributions from BIB-SEM and MICP are compared and the characteristics of pores associated with individual mineral phases are described. The nature of the pore systems that

105 controls two phase flow are also estimated, and relative roles of mineralogy on sealing capacity
106 are discussed.
107

108 2. Geological background and samples

109 The Zhanhua depression is one of the four major depressions in the Jiyang sub-basin, Bohai Bay
110 Basin (Fig. 1), bounded by the Chengdong uplift in the north and the Chenjiazhuang uplift in the
111 south, with an area of 3610 km^2 (Shi et al., 2005). It is a duplex half-graben rift basin controlled
112 by NE-SW and ENE-WSW trending extensional-shear faults, with many low uplifts and
113 half-grabens that are steep in the north and gentle in the south.
114 The Guantao formation (Ng) sits unconformably on underlying formations and was deposited
115 from 24.6 Ma, when the depression went into the post-rifting stage (Shi et al., 2005; Zhang et al.,
116 2004). The present depth is 1000 m to 1600 m, and it is currently at maximum burial. From top to
117 bottom, the Ng consists of two members, Ng_1 and Ng_2 (Shi et al., 2005; Zhang et al., 2004). The
118 lower Ng_2 represents mainly low stand alluvial fans and braided stream depositions, while the
119 sediments in the Ng_1 are characterised by a transition from braided stream to meandering stream
120 deposition (Zhang et al., 2004). The lower Ng_2, with a thickness of 200 - 500 m, is made up of
121 thick layers of block conglomerates and coarse sandstones, intercalated with green and red
122 mudstones and sandy mudstones. The upper Ng_1 is composed of red, purple, and gray-green
123 mudstones, sandy mudstones, and siltstone interbeds that are richer in clay near the top.
124 Furthermore, in silt-rich mudstones, the carbonate mineral content can be up to 26%. The stacked,
125 coarse sandy gravel rocks in the Ng_2 generally have excellent connectivity, providing storage
126 space for deep-sourced hydrocarbons. The uppermost Ng forms regional barriers for fluid flow,
127 whereas the mudstone interbedded with the sandy units in the Ng_1 act as local seals.
128 The samples collected are from the Ng_1 of two wells (Fig. 1B-C) and range from clay-rich
129 mudstone to silt-rich mudstone. X-ray diffraction (XRD) results show that the main minerals are
130 clay, quartz, K-feldspar, and plagioclase. Some silt-rich samples contain varying amounts of
131 carbonate minerals. Based on the mineral composition, four samples were selected for further
132 detailed study. Samples 1, 2, and 3, with 71%, 48%, and 30% of clay minerals, deposited in a
133 floodplain setting, were selected to study the pore systems of mudstones with different clay

content. Sample 4, located at the bottom of a channel, contains 21% clay minerals and 21% carbonate minerals (higher than most of the mudstones), and was selected to study the effect of carbonate minerals on the pore system and seal capacity.

3. Experimental methods

3.1 BIB-SEM

Samples were cut perpendicular to bedding with a blade in order to reveal the depositional and diagenetic characteristics. Samples were pre-polished using silicon carbide (SiC) and a Gatan 691 Precision Ion Polishing System (PIPS) used for argon broad ion beam milling. Polishing was undertaken with Ar ions in a vacuum (0.01 Pa) for 20 hours (angle 3°, 5 kV, 10-11 μA) to produce a high-quality cross-section. To prevent charging of the sample faces during SEM imaging, all polished samples were then coated with carbon with thicknesses of 15 - 25 nm.

The field emission SEM used for image acquisition is a SU-70 high resolution analytical SEM equipped with a secondary electron (SE) detector, a backscattered electron (BSE), as well as an Energy-dispersive X-ray spectroscopy (EDX) detector. SE images were acquired for documenting topographic variation, and BSE images were acquired for delineating compositional variation. EDS analyses of specific grains were also conducted for mineral identification. These analyses and images provided the basic microstructural and lithologic analysis, and to quantify the types and locations of pores (Loucks et al., 2012; Luo et al., 2019).

In order to obtain statistically significant and representative results, the REA for pore analysis was calculated using a box-counting method (Houben et al., 2013; Klaver et al., 2012) based on mineral composition (following the assumption that porosity is linked to mineralogy and mineral distribution). Element maps were gathered on areas around 10^6 μm^2 with the EDX detector. The settings for the EDX collection were set at 250 μs pixel dwell time, and 15 kV accelerating voltage. The obtained element images were then stitched together and converted to RGB colour mode mineral maps using AZtec software. Box counting started with an area (20 × 20 μm^2) selected at random, increasing by 10 μm in x and y directions for every following box. The relative contents of different minerals in each box are calculated by counting the pixel numbers of different colours. The area, where the individual contribution of each phase to the overall

composition does not significantly change, is considered as the REA.

For quantitative porosity analysis, large areas, based on REA, were selected to be imaged (SE) at magnifications of 10,000x (sample 2 - 4) or 20,000x (sample 1). SE images were taken at an acceleration voltage of 15 kV, with a working distance of 15 mm. The overlap was set as 23% to ensure that the obtained images covered all the selected area. Images were stitched together with the help of Adobe Photoshop software.

Pores are visualised in the SE images, characterised by the gray value pattern of a bright rim and a dark pore body (Houben et al., 2013). This feature makes it possible to identify pores with some automatic methods (such as thresholding, thresholding + edge detection, and watershed; Hemes et al.,2013; Hemes et al.,2016; Houben et al.,2014; Klaver et al.,2012; Klaver et al.,2015). However, there are also some problems with these automatic methods. As not all pores have a distinct and continuous boundary, some pores are not fully resolved. In addition, the internal grayscale features of large pores are inconsistent such that large pores are divided into a series of smaller pores. For these reasons, pores were outlined manually. The outlined pore areas were digitised with JMicrovision 1.2.7, and morphological parameters quantified for each segmented pore. The parameters used here to describe pore size and pore shape include the pore area (A_{pore}), pore perimeter (P), equivalent pore diameter (d_{eq}), pore short axis length (W), pore long axis length (L), axial ratio (W/L), and circularity ($4\pi A/P^2$). These pores are also classified based on their relationship to particles (Macquaker and Adams, 2003), and are classified according to the scheme from Desbois et al. (2009) and Heath et al. (2011). The classification divides the pores into interparticle pores that occur between particles (interP), and intraparticle pores that occur within particles (intraP). As pores smaller than 10 pixels (about 11 nm and 25 nm in diameter at 20,000× and 10,000×) could not be consistently and objectively detected, these pores are not included in the results. After digitisation, pores were all classified according to the minerals in which they occur.

To analyse the pore-area size distribution in different mosaics and samples, the pore data obtained from SEM was plotted as the logarithm of frequencies (N_i) of a certain pore area (S_{pore}) normalised by mosaic area (S_{mosaic}) and bin size(b_i) (Klaver et al., 2012).

$$\frac{N_i}{b_i \cdot S_{mosaic}} = C \cdot S_{pore}^{-D} \quad (1)$$

or alternatively:

$$\log\left(\frac{N_i}{b_i \cdot S_{mosaic}}\right) = -D \cdot \log(S_{pore}) + \log(C) \quad (2)$$

where N_i is the number of pores with pore area S_{pore} within bin b_i, where b_i doubles for subsequent bins ($b_1 = 1$ and $b_i = 2b_{i-1}$), S_{mosaic} is the area of the mosaic image, D is the power law exponent, and C is a constant of proportionality.

3.2 MICP

MICP was also carried out to compare with the BIB-SEM based pore data and to characterize the porosity and pore size distribution of bulk samples. MICP is a widely used technique for characterizing the distribution of pore throat sizes of porous materials (Hemes et al., 2013; Hildenbrand and Urai, 2003; Houben et al., 2014; Lai et al., 2018; Mathia et al., 2019). The method assumes that the porous network is represented by a bundle of interconnected, parallel, cylindrical tubes (Howard, 1991), and obtains the pore size distribution from the intruded volume of mercury at each pressure step, using the Washburn equation (Washburn, 1921). Samples were cut from the drill cores and dried at 50□ for 12 h. They were then placed in a sample cup filled with mercury in a pressure vessel. The applied pressure used for intrusion was slowly increased to 30,000 psi, corresponding to a pore throat diameter of 6 nm. The displacement pressure, which is that required to form a continuous, non-wetting phase-filled pore network, is routinely used for the estimation of capillary sealing efficiency of rocks (Schowalter, 1979). Threshold capillary entry pressures for the CH_4-H_2O system are also calculated, assuming a contact angle of 0° and an interfacial tension of 55.8 mN/m (Busch and Amann-Hildenbrand, 2013)

To compare MICP data and SEM data, raw MICP data were converted into frequencies of pore throat areas of a certain size (N_i^*) by separating the intruded mercury volume per pressure step by the size of pore throat diameter equivalent areas (Hemes et al., 2013). The same binning as for SEM data was also used for power law analysis:

$$\log\left(\frac{N_i^*}{b_i \cdot V_{total}}\right) = -D^* \cdot \log(S_{pore}^*) + \log(C^*) \quad (3)$$

where N_i^* is the frequencies of pore throats with pore area S_{pore}^* within bin b_i, V_{total} is the total volume of mercury intruded, D^* is the power law exponent, and C^* is a constant of proportionality.

4. Results

4.1. Qualitative description of microstructure

Sample 1 is the most clay-rich (71% clay minerals), comprising a clay matrix with some 5 - 30 μm diameter quartz, albite and K-feldspar grains 'floating' in the clay matrix (Fig. 2A). Samples 2 and 3 are coarser-grained and contain more and larger (up to 50 μm) non-clay minerals (mostly quartz) and much lower clay mineral contents (40% and 27%) than sample 1. As clay mineral content decreases, the size of non-clay mineral grains increases, and the morphology of non-clay mineral particles gradually changes from sub-rounded to sub-angular. In the images, these grains are touching each other, shifting the fabric from matrix-supported to grain-supported with increasing amounts of non-clay mineral grains (Fig. 2B-C). Sample 4 is a coarser-grained sample (grains up to 70 μm diameter) with 20% clay minerals and 21% calcite (Fig. 2D). Carbonate cement occurs in discrete patches and is usually enriched within large interparticle pores associated with larger non-clay minerals. Some non-clay minerals float within carbonate cement (Fig. 6H).

4.2. Mineralogy and pore morphology

In this study, similar major minerals were identified by BSE and EDX analyses in all four samples. These are quartz, K-feldspar, albite, and clay. In addition, sample 4 also has a relatively high content of calcite. Insignificant amounts of mica, Ca-feldspar and anatase were also encountered.

Interparticle pores in these samples include pores between non-clay minerals, and pores at interfaces between clay and non-clay minerals. The large pores are most commonly associated with coarser grains in more silt-rich samples, including quartz, K-feldspar and albite; they have characteristic equivalent diameters up to several microns (Fig. 4A, and 6A). Typically, a large number of interparticle pores are located at interfaces between clay and non-clay minerals with typical areas > 10^6 nm^2 in the fine-grained sample and up to 10^8 nm^2 in the coarse-grained samples (Fig. 3G, K, 4E, M, and 5A, I, K).

Intraparticle pores occur within the clay matrix and parts of the rigid grains. Pores within clay matrix show similar characteristics, such as elongated wedge to triangular or crescent shapes (Fig. 3A, C, D, 4O, P, and 6I). Although some interparticle pores in clay can be identified (Fig. 3D), it is difficult to separate all interparticle and intraparticle pores due to the physical size of clay minerals and the magnifications used in this study. Therefore, pores within the clay matrix are all

considered as intraparticle pores in this study. In silt-rich samples, there are large clay matrix pores (> 300 nm diameter) in areas rich in non-clay mineral grains (Fig. 4I, K, 5C, D, E). The equivalent diameters of intraparticle pores in albites and K-feldspars range from a few hundred nanometres to several microns (Fig. 3K, 4C, 5G, O and 6C). These intraparticle pores are elongated to roughly circular with jagged edges and lobate features on the inner pore wall. The morphologies of the intraparticle pores in K-feldspars are strongly influenced by the extent to which the grains have been dissolved. Pores in less dissolved grains have low width/length ratios, while those associated with more extensively dissolved grains, are rounded. The intraparticle pores in albites are generally larger than those in K-feldspars. Pores within mica grains are mainly present between mica lamellae, making these pores very elongated with smooth pore walls (Fig. 4M, 5M, and 6K). In the BSE images of sample 3 and sample 4, very bright interstratified minerals occur between the planes of micas (Fig. 2D, 5M, N, and 6K, L). Line scan results show that the bright minerals are rich in Fe and less in Si, Al, Mg, and K when compared with adjacent mica. The element characteristics of the bright areas suggest that it is chlorite. As the Guantao formation has never been buried deeply, the chlorite is probably the product of mica weathering.

Besides the pore types mentioned above, cracks are also observed in these samples, mainly within the clay matrix (Fig. 3A, E, 4Q, 5Q and 6J). The lengths of the cracks are between several microns to tens of microns and usually have low axial ratios, rough edges and sharp thin tips at both ends. Cracks are thought to have developed during sample coring and/or preparation and are not considered further.

4.3. Representative elementary area

Mineral compositional analysis based on BSE images and EDX maps show four main mineral phases in sample 1 (clay, quartz, K-feldspar and albite), five in samples 2 and 3 (clay, quartz, K-feldspar, albite, and mica), and seven in sample 4 (clay, quartz, K-feldspar, albite, mica, chlorite and calcite). Other mineralogical phases, such as mica (for sample 1), anatase, Ca-feldspar, and minerals that are not identified are classified as “others” in the determination of REAs. REA calculations based on mineralogy give the following results (Fig. 7): REA = 140 × 140 μm^2 for sample 2; REA = 160 × 160 μm^2 for sample 3; and REA = 230 × 230 μm^2 for sample 4. The mineral contents of sample 1 are stable when the area reaches 260 × 260 μm^2. As most of the

pores in sample 1 are relatively small, high magnification (20,000x) is required to study these pores in detail. Performing such a high magnification image analysis over such a large area is exceptionally time-consuming. Considering that (a) both quartz and K-feldspar are non-porous minerals, and (b) the relative contents of clay, non-porous minerals (quartz and K-feldspar) and porous minerals (albite) begins to stabilize at 100 × 100 μm^2, 100 × 100 μm^2 is taken as the representative area for sample 1. The clay contents obtained from EDX are all larger than those from XRD (20% at most), especially for the sample rich in clay. This may be partially caused by the limited spatial resolution of the BSE and EDX detectors (about few μm), and the fact that the element maps were scanned at a low magnification (700×). The detailed mineralogy of sub-micron grains in the clay matrix cannot by accurately classified using EDX (Klaver et al., 2012).

4.4. Quantification of porosity, pore size, and pore morphology by BIB-SEM

Single SE images were stitched together, and pores were all segmented manually. After segmentation and classification of minerals, the porosity distribution, and pore shape were studied and are summarised in Table 1. Cracks and pores below the PPR (practical pore detection resolution, 10 pixels) were not taken into account during the quantitative analysis. Total visible porosities within REAs ranges from 1.1% - 5.5%. The minimum pore area identified is about ~10^2 nm^2 (10 pixels at a magnification of 20,000×) and ~ 5 × 10^2 nm^2 (10 pixels at a magnification of 10,000×), while the maximum pore area varies from 10^6 nm^2 to 7 × 10^7 nm^2 with the decrease of clay content. Relatively small pores (3 × 10^3 - 10^4 nm^2) dominate the frequency distributions in all samples (Fig. 8). However, large pores, which account for very small proportion of total pores, contribute significantly to the total pore area. The contributions of pore areas to the total segmented porosities are either mono or bi-modally distributed. In detail, these peaks are located at ~10^5 nm^2 in sample 1, ~8 × 10^5 nm^2 in sample 3, and ~3 × 10^6 nm^2 in sample 4. Sample 2 does not have a clear peak in its porosity contribution distribution, but rather a wide range of pore sizes, contributing obviously to total segmented porosity. In addition, samples 2 and 4 also have a secondary peak in their porosity contribution distribution.

Numerically, the vast majority of pores occur within the clay matrix (Table 1); however, the contribution of clay-associated pores to the total porosity of different samples varies significantly. For the fine-grained sample (sample 1), pores within the clay matrix account for 90% of the total

visible porosity. In the coarser-grained samples (2 and 3), pores in the clay matrix contribute 53% - 45% of the total visible porosity, while in the coarsest sample (sample 4), about 34% of the total visible porosity occurs in the clay matrix. The average equivalent diameters of pores within the clay matrix are 106 nm, 127 nm, 135 nm, and 133 nm for samples 1, 2, 3, and 4. These pores have an average circularity in the range of 0.34 - 0.49, and average axial ratio varying from 0.28 - 0.35. The proportions of interparticle pores between grains increase from 0% to 34% with the decrease of clay content (Table 1). Interparticle pores are generally large (301 nm, 619 nm, and 1021 nm in average for sample 2, 3, and 4) and have high circularities (0.49, 0.50, 0.48), and axial ratios (0.41, 0.42, 0.49). Interparticle pores between clay and non-clay mineral grains (quartz, albite, K-feldspar, and mica) have diameters of several hundred nanometres, and low axial ratios and circularities. The interparticle pores associated with quartz, albite, K-feldspar and mica have average circularities in the range of 0.32 - 0.45, 0.37 - 0.47, and 0.34 - 0.46, and 0.31 - 0.45 while the average axial ratios range between 0.25 - 0.34, 0.30 - 0.34, 0.30 - 0.35, and 0.27 - 0.36 respectively. Interparticle pores between calcite and clay in sample 4 also have pores with low axial ratios (0.32 on average) and low circularities (0.40 on average), with an average diameter of 334 nm.

Albite can be very porous. Pores inside the albites can be up to several microns (Fig. 4C, 5G, and 6C) with average equivalent diameters from 151 nm to 237 nm (Table 1). The intraparticle pores of albites are roughly circular, with jagged edges and lobate features on the inner pore wall. They exhibit high circularities and axial ratios in the range of 0.52 - 0.60 and 0.40 - 0.45, respectively (Table 1). Compared with intraparticle pores in albites, intraparticle pores in K-feldspars are generally smaller in each sample, with average equivalent diameters ranging between 118 nm and 158 nm. The pores also have relatively low circularities (0.51 - 0.53) and low axial ratios (0.36 - 0.40). Pores in mica usually have low axial ratios (0.22 - 0.32) and low circularities (0.35 - 0.44). The presence of chlorite leads to the occurrence of more, smaller intraparticle pores, and the average pore size also decreases from 176 nm (sample 3) to 133 nm (sample 4).

4.5. MICP results

The porosities provided from corrected MICP data show the connected porosities are 7.5%, 13.7%, 17.9%, and 15.1% for sample 1, 2, 3, and 4 (Fig. 9A), which are much larger than those from

BIB-SEM. Volume porosity distributions, plotted as a function of pore throat size, show unimodal distributions for samples 1 and 2, and a bi-modal distribution for samples 3 and 4. Major peaks are found at pore throat diameters < 100 nm in the two fine-grained samples (samples 1 and 2), and ~150 nm, and ~300 nm for the two coarse-grained samples (samples 4 and 3) (Fig. 9B). The displacement pressures calculated from mercury intrusion data are 11.3 MPa, 6.6 MPa, 0.9 MPa, and 2.7 MPa for sample 1, 2, 3, 4 (Fig. 9C). Threshold capillary entry pressures for the CH_4-H_2O system,are 1.7 MPa, 1.0 MPa, 0.15 MPa, and 0.40 MPa for samples 1, 2, 3, and 4.

5. Discussion

5.1. Comparison of BIB-SEM and MICP data

Power laws, which have been used widely to describe the size distribution of grains, pores and soil-pore interfaces (Dathe et al., 2001; Desbois et al., 2009; Lipiec et al., 1998), have been previously applied to describe pore size distributions and to compare MICP pore throat distributions to BIB-SEM pore size data (Hemes et al., 2013; Houben et al., 2013; Klaver et al., 2012). The MICP data show an excellent linear relationship with $\log(S_{pore})$ between 3 and 8, and slopes start to decrease significantly at $\log(S_{pore})$ less than 3 (Fig. 10B, D, F, H). As mercury injection can result in a significant compression of the sample pore space (Hildenbrand and Urai, 2003) and closure of smaller pores (Klaver et al., 2015), this decrease may also be a function of the experimental process. For BIB-SEM data, slopes also decrease at low $\log(S_{pore})$ values (Fig. 10A, C, E, and G). The position where the slope of the trend line decreases is influenced by the magnification and thus the smallest pore that can be resolved. The slope of sample 1 start to fall at $\log(S_{pore})$ less than 2.9, while the slopes of sample 2, 3, and 4 start to decrease at $\log(S_{pore})$ less than 3.2, indicating the pores with diameter less than 40nm in sample 1 imaged at 10,000× and pores with diameter less than 50nm in sample 2, 3, and 4 imaged at 20,000× are not fully resolved. Neither the BIB-SEM data nor the MICP data can fully detect the small pores close to their resolution.

There are notable differences when comparing all data from MICP and BIB-SEM directly. However, the MICP and BIB-SEM data do have very similar power law exponents for the pores in a specific range (red squares in Fig. 10). In sample 1, points with $\log(S_{pore})$ values between 3 and

5.5 from SEM data have similar power law exponent to those with log(S_{pore}) values between 3 and 8 from MICP data (Fig. 10A and B). In samples 2, 3 and 4, the power law exponent of points with log(S_{pore}) between 3 and 6 are very similar with the exponents from MICP data, with log(S_{pore}) between 3 and 8 (Fig. 10C-H). The similarity values for the power law exponents based on SEM and MICP suggests the occurrence of a tube-like pore network (Houben et al., 2014). Areas larger than 10^3 nm^2 in this study are thus well connected.

Mosaic area also impacts the BIB-SEM pore size distribution results, especially for large pores. As shown in Fig. 10C, E, and G, the points of sample 2, 3, and 4 with log(S_{pore}) values larger than 6 are all deviated from the line, however, the points are closer to the line with the increase of the mosaic area (e.g. the point with log(S_{pore}) value of 7 in sample 4 is closer to the line than that of sample 3, while the same point in sample 3 is closer than that of sample 2). More points follow the power law distribution with an increase of mosaic area. The number of pores in samples 2, 3, and 4, obtained from SEM images, with areas between 10^6 nm^2 and 10^7 nm^2, account for 37%, 46%, and 61% of the pores estimated from the fitted lines. The incomplete detection of large pores may be caused by two reasons. Firstly, pores at boundaries of the mosaic areas may not be fully detected, which may lead to a significant effect in the final result. Furthermore, the results may also be affected by sample heterogeneity. Even though the mosaic area obtained from the box-counting method is representative of mineral abundance, pore data obtained from mosaics based on REA may still not contain statistically significant information for these relatively large pores, which is affected by the assemblage of particles. In order to obtain more accurate information of relatively large pores, more pores within an area that exceeds the mineral-based REA should be counted in the future. Since more large pores are characterized in sample 4 than in sample 3, this may explain why the main peak of sample 3 is larger than that of sample 4 in MICP data, while the main peak in sample 3 is smaller than that of sample 4 in the BIB-SEM data. In addition, differences between the porosity obtained by SEM and that by MICP may also be related to the incomplete detection of these large pores.

5.2. Effect of mineralogy on porosity, pore size distribution, and pore morphology

Samples with different mineral compositions and particle size compositions have significantly different pore characteristics. To better illustrate the impact of mineral composition, the differences in pore characteristics between samples 1 to 3 (comprising only detrital terrigenous grains) are first compared, and then the effect of carbonate cement is discussed.

Higher contents of silt-grade, non-clay minerals cause a switch from a clay matrix-supported to a grain-supported framework (Fig. 2 A-C). Interactions between silt particles change the unimodal pore size distributions to bimodal pore size distributions (Fig. 9B) (Aplin and Moore, 2016; Dewhurst et al., 1999). With the magnifications used in this study, SEM-visible porosity increases with decreasing clay mineral contents, and the contribution of interparticle pores to the visible porosity increases significantly (Table 1 and Fig. 11). The interaction of silt particles also leads to stress shadows, resulting in a less compacted clay matrix (Philipp et al., 2017; Schneider et al., 2011), and different pore size distributions. The data obtained from SEM show that the power law exponents of pores within clay, and interparticle pores at the interface between non-clay minerals and clay matrix in samples 1, 2, and 3, decrease with increasing non-clay mineral contents (Fig. 12 A and B). At the same time, the average diameter of these pores increases (Table 1), indicating that the pores both within the clay matrix and at the interface between non-clay minerals and clay matrix, are enriched in larger pores. In addition, pores within the less compacted clay matrix of samples 2 and 3 have higher proportions of more rounded pores (Table 1 and Fig. 13). The variations in the degree of compaction of the clay minerals are very similar to the results calculated by clay packing density (1 - porosity)/[1 - non-clay volume fraction]) proposed by Bobko and Ulm (2008). Higher porosities and higher non-clay volume fractions lead to lower clay packing densities. This may also explain why SEM-visible clay matrix porosity does not decrease with a decrease in clay mineral content (Fig. 11). However, as clay matrices within mudstones include large volumes of pores which cannot be resolved at the magnifications used in this study (Dewhurst et al., 1999; Mathia et al., 2019), the total volume of clay matrix porosity is likely to decrease as the content of clay minerals decreases.

Dissolution has also influenced the porosity and pore size distribution of the samples. Unstable silicates, including albite, K-feldspar and mica, are subject to dissolution. The contribution of intraparticle pores within albite can sometimes be higher than that of interparticle pores between

clay matrix and albite grains (sample 2 in Table 1). Intraparticle pores can be as large as several microns in silt-rich samples (Fig. 4C, Fig. 5G). However, the average pore size does not increase with increasing content of non-clay volume fraction. The presence of a large number of small pores is probably the main reason for the decrease in the average pore size (Table 1). Dissolution pores in albite and K-feldspar have higher circularities and axial ratios (Table 1 and Fig. 13). The degree of dissolution of albites and the sizes of resultant intraparticle pores are usually larger than those within K-feldspar, which may be due to the different kinetic rate constants of dissolution reactions for different minerals (White et al., 2001). Although some albites have undergone severe dissolution and developed large intraparticle pores, on a macroscopic level, most of the rigid grains have not undergone serious dissolution and the intraparticle pores are relatively small and isolated. Thus, the intraparticle pores act more as storage spaces rather than flow spaces.

Compared to sample 3, carbonate-cemented sample 4 has lower porosity. Non-porous calcite fills the pore space, especially large interparticle pores between non-clay minerals (Fig. 6F, H), reducing total porosity. As shown in Fig. 12C, points in sample 4 with $\log(S_{pore})$ values between 3 and 6.2 have a low power law exponent, and the slope starts to fall dramatically when $\log(S_{pore})$ is larger than 6.2, indicating that the presence of carbonate cement leads to a significant decrease in the proportion of large pores with areas greater than 10^6 nm^2. Although the slope variation may be related to the insufficient mosaic area, as discussed before, such a pronounced variation is more likely to reflect the filling of large pores by cementation. In addition, the interparticle pores between non-clay minerals in sample 4 have a larger proportion of pores with higher axial ratios and circularities than sample 3 (Fig. 13), which may also suggest that most of these pores are not affected by cementation. BSE petrography (Fig. 14) shows that calcite cementation occurred before compaction. The paleoclimate during sedimentation of the Guantao Formation transitioned from early warm and humid to the late-stage drought, indicated by the characteristics of preserved biota, and mudstone colour (Dai et al., 1994). Near-surface, eogenetic carbonate cementation in fluvial deposits is closely related to semiarid climatic condition (Morad et al., 1998; Morad et al., 2010), which leads to lesser cementation of interparticle pores.

The development of contact cements in sample 4 also inhibits compaction by forming a stiffer framework (Fabricius et al., 2008; Mathia et al., 2016), resulting in a pore system within the clay

matrix with a lower power law exponent and a larger mean value of pore diameter (Table 1 and Fig. 12A). However, the volume of pores at the interface between clay and non-clay minerals of sample 4 is smaller than that of sample 3 (Fig. 11), while the power law exponent is higher, indicating that the proportion of relatively large pores in sample 4 is smaller than that in sample 3 (Fig. 12B). Considering that (a) the pores at the interface between non-clay minerals and clay still have high proportion of pores with high elongations and axial ratios (Fig. 13), and (b) clay matrix pores have undergone less compaction, it is cementation, rather than compaction, that is probably the main cause of the reduction in pore volumes between clay and non-clay minerals.

5.3. Implications for seal capacity

The displacement pressures calculated from mercury intrusion of sample 1 to 4 imply that the minimum pore size diameters that connects to allow flow of the non-wetting phase across the mudstone are about 110 nm, 190 nm, 1340 nm, and 470 nm respectively. This corresponds to about 20%, 13%, 6%, and 8%, of the porosity that would be saturated with the non-wetting phase. Although the SEM cannot identify extremely small pores, almost all the pores that provide the initial connectivity for two phase flow can be observed by SEM. The proportions of pores, larger than the critical diameter, in each phase and their contribution to the connected network at the critical diameter are presented in Fig. 15 B and A. The nature of the critically connected pore network varies significantly as a function of mineralogy and grain size. For clay matrix-supported sample 1, clay matrix pores are the main component of the critically-connected pore system (Fig, 11) and thus control seal capacity and initial leakage (Fig. 15A). With increasing proportions of coarser, non-clay minerals, more interparticle pores between clay and non-clay minerals occur and exert a stronger control on capillary breakthrough and the onset of two phase flow. When the framework becomes grain-supported (sample 3), the capillary breakthrough is primarily through larger interparticle pores located between (a) non-clay minerals and (b) clay and non-clay minerals (Fig. 15 B). Only a small portion of clay matrix pores participate in the formation of the network at capillary breakthrough (Fig. 15 B) and contribute very slightly to it (Fig. 15 A). Calcite cements reduce pore space (Fig. 9 A and 11) and the calcite-cemented sample 4 has a high proportion of interparticle pores between (a) non-clay minerals and (b) clay and non-clay minerals (Fig. 11).

However, these pores are not sufficiently connected to allow capillary breakthrough, so that breakthrough requires invasion of part of the porosity associated with the clay matrix (Fig. 15). This explains the elevated breakthrough pressure for the carbonate-bearing silty mudstone. With increasing cementation, more interparticle pores between non-clay minerals, and at interfaces between clay matrix and non-clay minerals will be filled, so that the formation of a connected network by the non-wetting phase fluid will require higher capillary pressures to connect smaller clay matrix pores. More highly cemented siltstones are likely to have higher seal capacities. In the silty mudstones and fine sandstones of the Guantao formation, carbonate contents are usually less than 20% and breakthrough pressures do not exceed 0.4 MPa; in this case, carbonate cementation in the Zhanhua depression is insufficient for these rocks to become effective barriers to two phase flow.

Overall, clay mineral content is the most important control on the sealing ability of shallow fluvial mudstone in the Zhanhua depression; carbonate cements reduce porosity but the seal capacity of cemented siltstone is still low.

6. Conclusions

1. Pore areas inferred from BIB-SEM measurements on mineralogically-defined REAs follow similar power law distributions to MICP porosimetry, within the range of diameters over which the BIB-SEM magnification captures the full pore system. At a given magnification, pores smaller than a given diameter are not imaged, and insufficient pores with diameters above a certain limit may be imaged to generate statistically significant information from a mineralogically-defined REA. The similar power law exponents indicate that pores with areas larger than 10^3 nm^2 are well-connected.
2. Higher silt contents cause a switch from matrix-supported to grain-supported frameworks, and pores between grains contribute more significantly to total porosities. Compared to matrix supported mudstones, pores within the clay-matrix and pores at interfaces between grains are larger, while there is also an increased proportion of pores with high axial ratios and circularities as a consequence of more effective force chains between larger grains. With the decrease in clay content, capillary breakthrough and the development of a pore network

for the flow of the non-wetting phase, changes from pores within the clay matrix, to interparticle pores.

3. Carbonate cements reduce porosity in more silt-rich mudstones by partially filling (a) interparticle pores between non-clay minerals and clay, and (b) pores between non-clay minerals with areas larger than 10^6 nm^2. Cementation of larger pores increases seal capacity locally and means that capillary breakthrough requires connectivity of relatively small pores within the clay matrix. Nevertheless, clay content is the most important control on mudstone seal capacity in the Zhanhua depression, because carbonate cement is generally less than 20%, insufficient to enable silt-rich mudstones to retain significant hydrocarbon columns.

Acknowledgements

This work is supported by Nation Science and Technology Major Project of the Ministry of Science and Technology of China (2016ZX05006-007; 2016ZX05001-001), SINOPEC (P15084), the Fundamental Research Funds for the Central Universities (17CX02006A) and China Scholarship Council (201706450082). ACA's work is supported via the UK Natural Environment Research Council grant number NE/R017840/1. We would like to thank Shengli Oil field, SINOPEC for the help of sample collection. We also thank Editor Dr. Hugh Daigle and two anonymous reviewers for their valuable comments which helped to improve the quality of the manuscript.

References:

Allen, M. B., Macdoland, D., Xun, Z., Vincent, S. J., Brouet-Menzies, C., 1997. Early Cenozoic two-phase extension and late Cenozoic thermal subsidence and inversion of the Bohai Basin, northern China. Mar. Petrol. Geol. 14, 951-972.

Aplin, A.C., Macquaker, J.H., 2011. Mudstone diversity: Origin and implications for source, seal, and reservoir properties in petroleum systems. AAPG Bull. 95, 2031-2059.

Aplin, A.C., Matenaar, I.F., McCarty, D.K., Van der Pluijm, B.A., 2006. Influence of mechanical compaction and clay mineral diagenesis on the microfabric and pore-scale properties of deep-water Gulf of Mexico mudstones. Clays Clay Miner. 54, 500-514.

Aplin, A.C., Moore, J.K.S., 2016. Observations of pore systems of natural siliciclastic mudstones. The Clay Miner. Soc. Workshop Lect. Ser. 21, 31–42.

Armitage, P.J., Worden, R.H., Faulkner, D.R., Aplin, A.C., Butcher, A.R., Espie, A.A., 2013. Mercia Mudstone Formation caprock to carbon capture and storage sites: petrology and petrophysical characteristics. J. Geol. Soc. London 170, 119-132.

Armitage, P.J., Worden, R.H., Faulkner, D.R., Aplin, A.C., Butcher, A.R., Illiffe, J., 2010. Diagenetic and sedimentary controls on porosity in Lower Carboniferous fine-grained lithologies, Krechba field, Algeria: A petrological study of a caprock to a carbon capture site. Mar. Pet. Geol. 27, 1395-1410.

Bobko, C., Ulm, F.J., 2008. The nano-mechanical morphology of shale. Mech. Mater. 40, 318-337.

Busch, A., Amann-Hildenbrand, A., 2013. Predicting capillarity of mudrocks. Mar. Pet. Geol. 45, 208-223.

Dai, Q., Di, M., Guo, J., Li, J., He, L., Jia, J., 1994. Sedimentary facies research of the Neogene in the Jiyang Depression. Geological Review, 40, 8-18 (in Chinese with English abstract)

Dathe, A., Eins, S., Niemeyer, J., Gerold, G., 2001. The surface fractal dimension of the soil–pore interface as measured by image analysis. Geoderma 103, 203-229.

Davy, C.A., Skoczylas, F., Lebon, P., Dubois, T., 2009. Gas migration properties through a bentonite/argillite interface. Appl. Clay Sci. 42, 639-648.

Desbois, G., Urai, J.L., Kukla, P.A., 2009. Morphology of the pore space in claystones–evidence

561 from BIB/FIB ion beam sectioning and cryo-SEM observations. eEarth Discuss. 4, 1-19.
562 Dewhurst, D.N., Aplin, A.C., Sarda, J.P., 1999. Influence of clay fraction on pore□scale properties
563 and hydraulic conductivity of experimentally compacted mudstones. J. Geophys. Res.: Solid Earth
564 104, 29261-29274.
565 Dewhurst, D.N., Jones, R.M., Raven, M.D., 2002. Microstructural and petrophysical
566 characterization of Muderong Shale: application to top seal risking. Pet. Geosci. 8, 371-383.
567 Downey, M.W., 1984. Evaluating seals for hydrocarbon accumulations. AAPG Bull. 68,
568 1752-1763.
569 Fabricius, I. L., Gommesen, L., Krogsbøll, A., Olsen, D., 2008. Chalk porosity and sonic velocity
570 versus burial depth: Influence of fluid pressure, hydrocarbons, and mineralogy. AAPG Bull. 92,
571 201-223.
572 Heath, J. E., Dewers, T. A., McPherson, B. J.O.L., Petrusak, R., Chidsey, T. C., Rinehart, A. J.,
573 Mozley, P. S., 2011. Pore networks in continental and marine mudstones: Characteristics and
574 controls on sealing behavior. Geosphere 7, 429-454.
575 Hemes, S., Desbois, G., Klaver, J., Urai, J.L., 2016. Microstructural characterisation of the
576 Ypresian clays (Kallo-1) at nanometre resolution, using broad-ion beam milling and scanning
577 electron microscopy. Neth. J. Geosci. 95, 293-313.
578 Hemes, S., Desbois, G., Urai, J.L., De Craen, M., Honty, M., 2013. Variations in the morphology
579 of porosity in the Boom Clay Formation: insights from 2D high resolution BIB-SEM imaging and
580 Mercury injection Porosimetry. Neth. J. Geosci. 92, 275-300.
581 Hildenbrand, A., Urai, J.L., 2003. Investigation of the morphology of pore space in
582 mudstones—first results. Mar. Pet. Geol. 20, 1185-1200.
583 Houben, M.E., Desbois, G., Urai, J.L., 2013. Pore morphology and distribution in the Shaly facies
584 of Opalinus Clay (Mont Terri, Switzerland): Insights from representative 2D BIB–SEM
585 investigations on mm to nm scale. Appl. Clay Sci. 71, 82-97.
586 Houben, M.E., Desbois, G., Urai, J.L., 2014. A comparative study of representative 2D
587 microstructures in Shaly and Sandy facies of Opalinus Clay (Mont Terri, Switzerland) inferred
588 form BIB-SEM and MIP methods. Mar. Pet. Geol. 49, 143-161.
589 Howard, J.J., 1991. Porosimetry measurement of shale fabric and its relationship to illite/smectite

590 diagenesis. Clays Clay Miner. 39, 355-361.
591 Hu, G., Yang, R., Wang, L., Hu, W., Cao, J., 2019. Hydrocarbon potential and depositional
592 environment of the Lower Cretaceous black mudstones and shales in the coastal Guangdong
593 Province, China. Mar. Pet. Geol. 99, 92-106.
594 Klaver, J., Desbois, G., Urai, J.L., Littke, R., 2012. BIB-SEM study of the pore space morphology
595 in early mature Posidonia Shale from the Hils area, Germany. Int. J. Coal Geol. 103, 12-25.
596 Klaver, J., Desbois, G., Littke, R., Urai, J.L., 2015. BIB-SEM characterization of pore space
597 morphology and distribution in postmature to overmature samples from the Haynesville and
598 Bossier Shales. Mar. Pet. Geol. 59, 451-466.
599 Klaver, J., Hermes, M., Houben, M., Desbois, G., Radi, Z., Urai, J.L. 2015. The connectivity of
600 pore space in mudstones: insights from high□pressure Wood's metal injection, BIB□SEM
601 imaging, and mercury intrusion porosimetry. Geofluids 15, 577-591.
602 Lai J., Wang G., Wang Z., Chen J., Pang X., Wang S., Zhou Z., He Z., Qin Z., Fan Z., 2018. A
603 review on pore structure characterization in tight sandstones. Earth-Sci. Rev. 177, 436-457.
604 Lai J., Wang G., Shi Y., Zhao T., Pang X., Fan X., Qin Z., Fan X., 2019. Pore structure and fractal
605 characteristics of Ordovician Majiagou carbonate reservoirs in Ordos Basin, China. AAPG Bull.,
606 103, 2573-2596.
607 Lipiec, J., Hatano, R., Słowińska-Jurkiewicz, A., 1998. The fractal dimension of pore distribution
608 patterns in variously-compacted soil. Soil Tillage Res. 47, 61-66.
609 Loucks, R.G., Reed, R.M., Ruppel, S.C., Jarvie, D.M., 2009. Morphology, genesis, and
610 distribution of nanometer-scale pores in siliceous mudstones of the Mississippian Barnett Shale. J.
611 Sediment. Res. 79, 848-861.
612 Loucks, R.G., Reed, R.M., Ruppel, S.C., Hammes, U., 2012. Spectrum of pore types and networks
613 in mudrocks and a descriptive classification for matrix-related mudrock pores. AAPG Bull. 96,
614 1071-1098.
615 Lu, J., Milliken, K., Reed, R.M., Hovorka, S., 2011. Diagenesis and sealing capacity of the middle
616 Tuscaloosa mudstone at the Cranfield carbon dioxide injection site, Mississippi, USA. Environ.
617 Geosci. 18, 35-53.
618 Luo L., Meng W., Gluyas J., Tan X., Gao X., Feng M., Kong X., Shao H., 2019. Diagenetic

characteristics, evolution, controlling factors of diagenetic system and their impacts on reservoir quality in tight deltaic sandstones: Typical example from the Xujiahe Formation in Western Sichuan Foreland Basin, SW China. Mar. Pet. Geol. 103, 231-254.

Macquaker, J.H., Adams, A.E., 2003. Maximizing information from fine-grained sedimentary rocks: An inclusive nomenclature for mudstones. J. Sediment. Res. 73, 735-744.

Mathia, E. J., Bowen, L., Thomas, K. M., Aplin, A. C., 2016. Evolution of porosity and pore types in organic-rich, calcareous, Lower Toarcian Posidonia Shale. Mar. Pet. Geol. 75, 117-139.

Mathia, E.J., Rexer, T.F.T., Thomas, K.M., Bowen, L., Aplin, A.C., 2019. Influence of clay, calcareous microfossils, and organic matter on the nature and diagenetic evolution of pore systems in mudstones. J. Geophys. Res.: Solid Earth 124, 149-174

McCreesh, C.A., Ehrlich, R., Crabtree, S.J., 1991. Petrography and reservoir physics II: relating thin section porosity to capillary pressure, the association between pore types and throat size. AAPG Bull. 75, 1563-1578.

Meng, M., Ge, H., Shen, Y., Hu, Q., Li, L., Gao, Z., Tian T., Chao, J., 2020. The effect of clay-swelling induced cracks on imbibition behavior of marine shale reservoirs. J. Nat. Gas Sci. Eng. 83, 103525.

Meng, M., Ge, H., Shen, Y., Li, L., Tian, T., Chao, J., 2020. The effect of clay-swelling induced cracks on shale permeability during liquid imbibition and diffusion. J. Nat. Gas Sci. Eng. 83, 103514.

Morad, S., Al-Ramadan, K., Ketzer, J.M., De Ros, L.F., 2010. The impact of diagenesis on the heterogeneity of sandstone reservoirs: A review of the role of depositional facies and sequence stratigraphy. AAPG Bull. 94, 1267-1309.

Morad, S., De Ros, L.F., Nystuen, J.P., Bergan, M., 1998. Carbonate cementation in sandstones: distribution patterns and geochemical evolution, in Morad, S., ed., Carbonate Cementation in Sandstones: Distribution Patterns and Geochemical Evolution. Spec. Publ. Int. Assoc. Sedimentol. 26, 53-86.

Pang, Z., Li, Y., Yang, F., Duan, Z., 2012. Geochemistry of a continental saline aquifer for CO_2 sequestration: The Guantao formation in the Bohai Bay Basin, North China. Appl. Geochem. 27, 1821-1828.

Philipp, T., Amann-Hildenbrand, A., Lacurich, B., Desbois, G., Littke, R., Urai, J.L., 2017. The effect of microstructural heterogeneity on pore size distribution and permeability in Opalinus Clay (Mont Terri, Switzerland): insights from an integrated study of laboratory fluid flow and pore morphology from BIB-SEM images. Geol. Soc. London, Spec. Publ. 454, 85-106.

Schneider, J., Flemings, P.B., Day-Stirrat, R.J., Germaine, J.T., 2011. Insights into pore-scale controls on mudstone permeability through resedimentation experiments. Geology 39, 1011-1014.

Schowalter, T.T., 1979. Mechanics of secondary hydrocarbon migration and entrapment. AAPG Bull. 63, 723-760.

Shi, D., Li, M., Pang, X., Chen, D., Zhang, S., Wang, Y., Jin, Q., 2005. Fault-fracture mesh petroleum plays in the Zhanhua Depression, Bohai Bay Basin: Part 2. Oil-source correlation and secondary migration mechanisms. Org. Geochem. 36, 203-223.

Sigal, R.F., 2009. A methodology for blank and conformance corrections for high pressure mercury porosimetry. Meas. Sci. Technol. 20, 045108.

Underwood, E.E., 1970. Quantitative stereology. Addison-Wesley, pp. 80-93.

Washburn, E.W., 1921. Note on a method of determining the distribution of pore sizes in a porous material. Proc. Natl. Acad. Sci. Unit. States Am. 7, 115-116.

White, A.F., Bullen, T.D., Schulz, M.S., Blum, A.E., Huntington, T.G., Peters, N.E., 2001. Differential rates of feldspar weathering in granitic regoliths. Geochim. Cosmochim. Acta 65, 847-869.

Yang, Y., Aplin, A.C., 1998. Influence of lithology and compaction on the pore size distribution and modelled permeability of some mudstones from the Norwegian Margin. Mar. Pet. Geol. 15, 163-175.

Zhang, L., Lu, S., Xiao, D., Li, B., 2017. Pore structure characteristics of tight sandstones in the northern Songliao Basin, China. Mar. Pet. Geol. 88, 170-180.

Zhang, S., Wang, Y., Shi, D., Xu, H., Pang, X., Li, M., 2004. Fault-fracture mesh petroleum plays in the Jiyang Superdepression of the Bohai Bay Basin, eastern China. Mar. Pet. Geol. 21, 651-668.

Zhu, G., Zhang, S., Jin, Q., Dai, J., Zhang, L., Li, J., 2005. Origin of the Neogene shallow gas accumulations in the Jiyang Superdepression, Bohai Bay Basin. Org. Geochem. 36, 1650-1663.

Table 1 Total visible porosity of different samples, and the contribution to the porosity for the differentiated minerals and mineral aggregates.

Sample	Magnification	Images analysed	Area Imaged (μm^2)	Number of pores detected	Visible porosity (%)	Mineral phase	Number of pores detected in mineral phase	Contribution to total porosity (%)	Average pore size (d_{eq} in nm)	80% of pore have d_{eq}<(nm)	Circularity (mean)	Axial ratio (mean)
1	20,000	630	10000	5910	1.1	Clay (Intra)	5551 (5551)	89.9	106	154	0.34	0.28
						Albite (Inter/Intra)	29 (19/10)	0.8 (0.7/0.1)	(150/110)	(265/128)	(0.43/0.38)	(0.31/0.27)
						K-feldspar (Inter)	61 (61)	1.9	148	181	0.34	0.31
						Quartz (Inter)	255 (255)	7.1	145	226	0.32	0.25
						Others	14	0.3	/	/	/	/
2	10,000	432	19600	13205	2.2	Clay (Intra)	10235 (10235)	52.7	127	178	0.42	0.31
						Albite (Inter/Intra)	965 (435/530)	18.54 (8.1/10.3)	(251/237)	(367/339)	(0.37/0.52)	(0.30/0.42)
						K-feldspar (Inter)	481 (481)	5.8 (5.8)	216	316	0.39	0.30
						Quartz (Inter)	1110 (1110)	13.8 (13.8)	208	309	0.39	0.30
						Mica (Inter)	38 (38)	0.6 (0.6)	261	410	0.31	0.27
						Non-clay minerals (Inter)	114 (114)	3.21 (3.2)	301	391	0.49	0.41
						Others	262	5.6%	/	/	/	/
3	10,000	960	25600	29125	5.5	Clay (Intra)	22467 (22467)	44.5	135	187	0.49	0.35
						Albite (Inter/Intra)	1984 (726/1258)	12.2 (7.7/4.5)	(300/177)	(425/249)	(0.44/0.55)	(0.33/0.40)
						K-feldspar (Inter/Intra)	2518 (691/1827)	10.7 (6.0/4.7)	(296/158)	(418/222)	(0.45/0.53)	(0.33/0.40)
						Quartz (Inter/Intra)	1345 (1212/133)	11.3 (11.1/0.2)	(291/130)	(425/173)	(0.45/0.61)	(0.34/0.42)
						Mica (Inter/Intra)	305 (148/157)	2.2 (1.7/0.5)	(362/176)	(544/253)	(0.45/0.44)	(0.36/0.32)
						Non-clay minerals (Inter)	300 (300)	17.9	619	906	0.50	0.42
						Others	206	1.2%	/	/	/	/
4	10,000	1,200	62500	32575	3.8	Clay (Intra)	26158 (26158)	34.0	133	186	0.47	0.32
						Albite (Inter/Intra)	1778 (725/1053)	6.0 (4.2/1.8)	(237/151)	(328/213)	(0.47/0.60)	(0.34/0.45)
						K-feldspar (Inter/Intra)	745 (473/272)	3.1 (2.9/0.2)	(268/118)	(364/160)	(0.46/0.51)	(0.35/0.36)
						Quartz (Inter/Intra)	1256 (1004/252)	12.1 (11.7/0.4)	(303/124)	(373/134)	(0.44/0.56)	(0.34/0.39)
						Mica (Inter/Intra)	1519 (160/1359)	3.0 (1.1/1.9)	(316/133)	(454/179)	(0.39/0.35)	(0.30/0.22)
						Calcite (Inter)	395 (395)	4.4	334	453	0.40	0.32
						Non-clay minerals (Inter)	480 (480)	37.1	1021	1655	0.48	0.49
						Others	244	0.5	/	/	/	/

Total pore number corrected for the cracks and pores below the PPR (practical pore detection resolution, 10 pixels)

Axial ratio = W/L; Squared circularity = $4\pi A/P^2$. Where W = Pore short axis length, L = Pore long axis length, A = Pore area, P = Pore perimeter

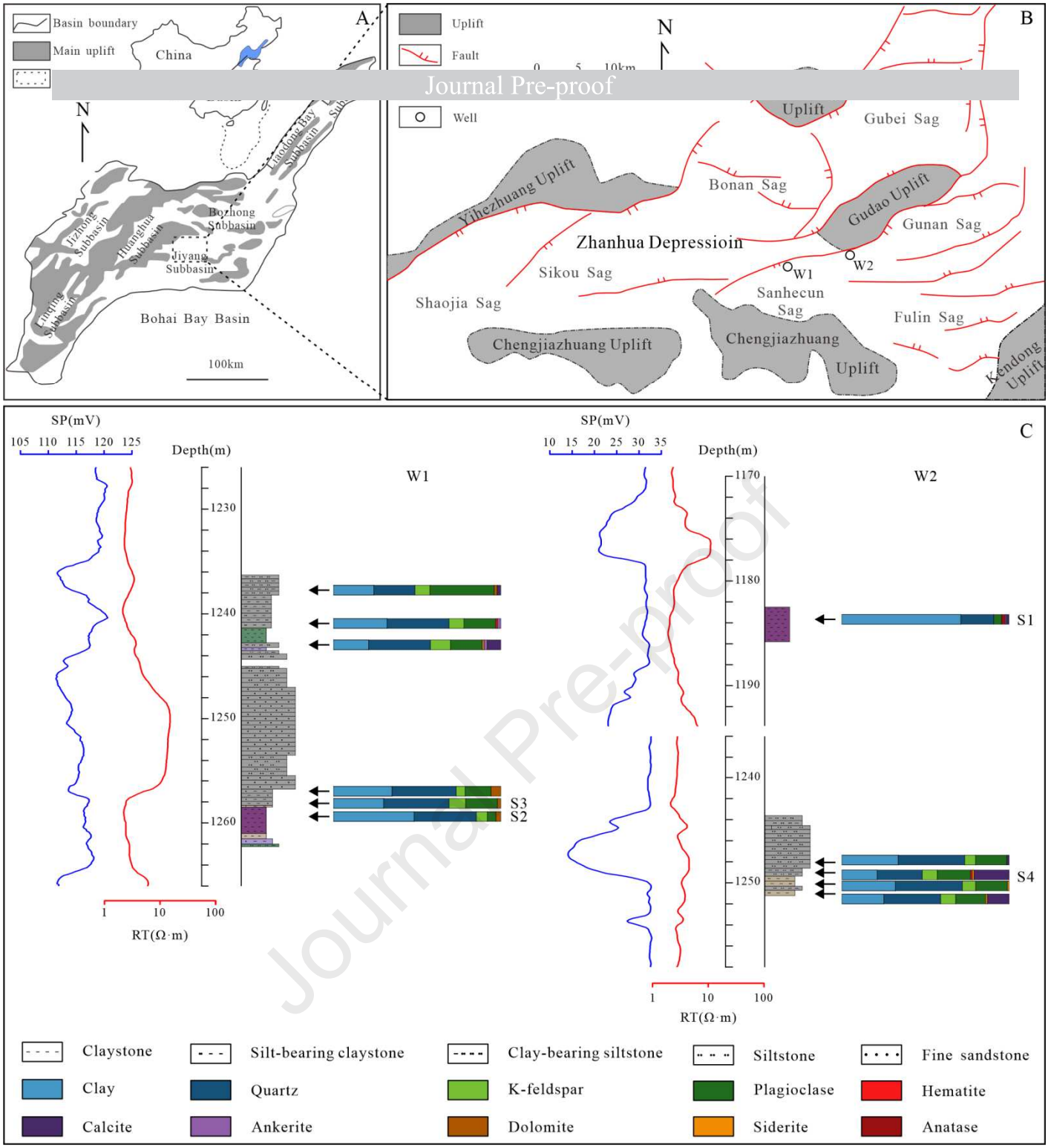

Fig. 1. Location of the study area and sample location. A. Sub-basins of Bohai Bay Basin (sub-basin classification from (Allen et al., 1997). B. Simplified structural map of the Zhanhua Depression and the location of sampled wells. C. Sample locations and mineralogy.

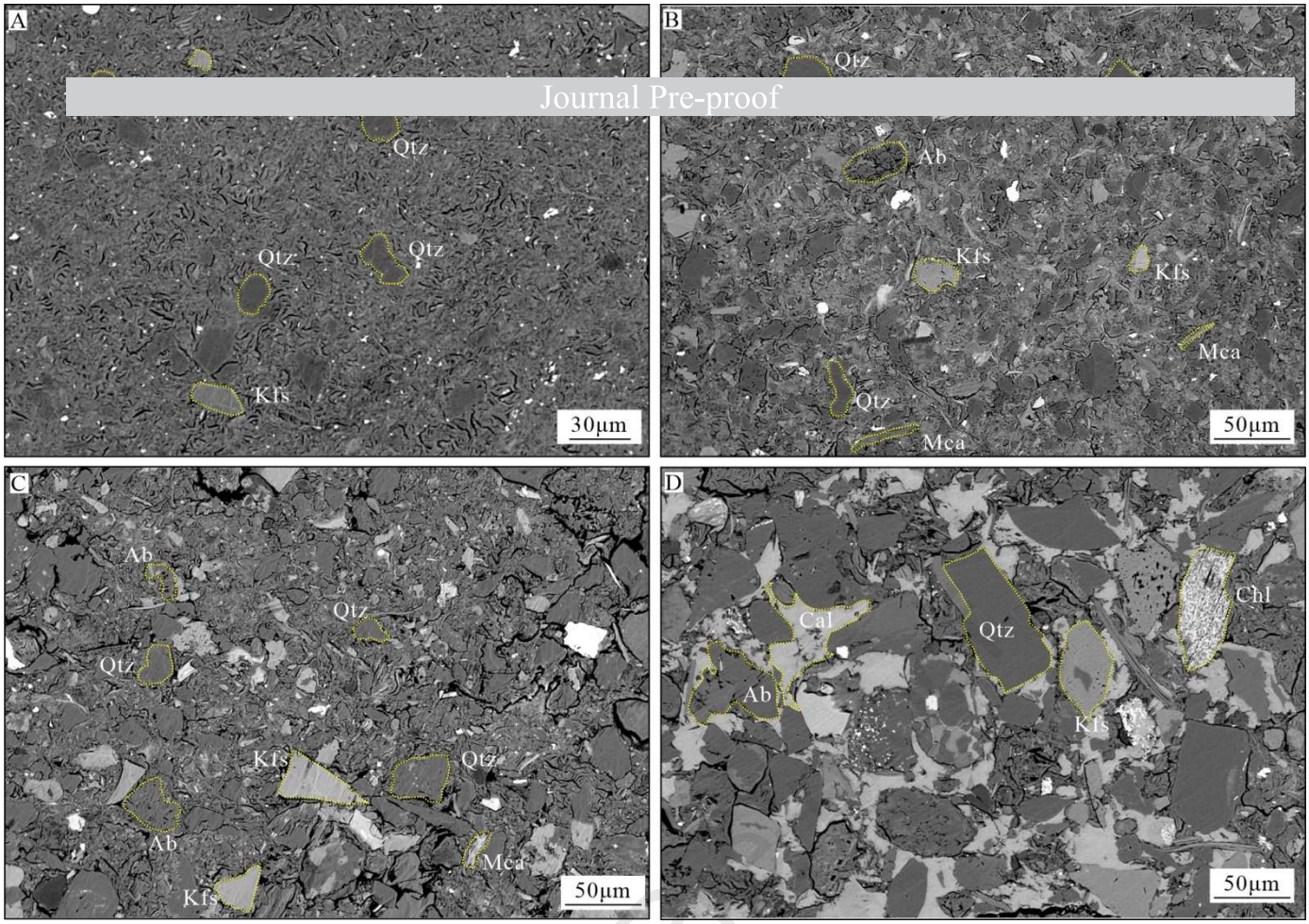

Fig. 2 Overview of typical microstructures in BSE mode. Figures A to D correspond to samples 1 to 4, respectively, and minerals are marked with yellow borders. Abbreviations used: Qtz=Quartz, Kfs=K-feldspar, Ab=Albite, Cal=Calcite, Mca=Mica, Ch=Chlorite.

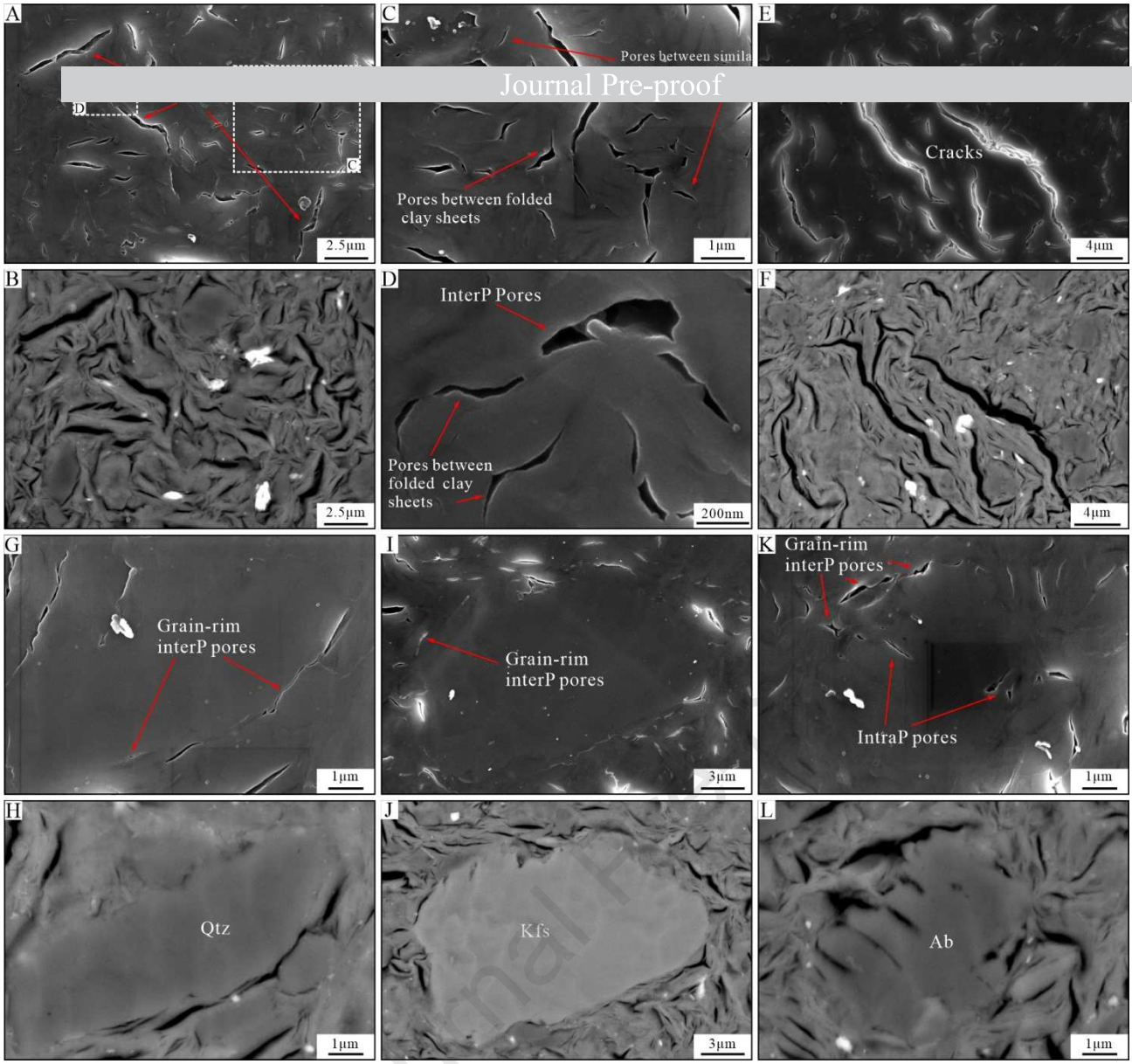

Fig. 3. Sample 1: SE and BSE images of common minerals and associated pores.

A. SE micrograph of the clay matrix with pores. B. BSE image of A. C and D. Enlargement of two parts of the micrograph shown in A. Pores in the clay matrix can be divided into two types: (i) elongated pores between similarly oriented clay sheets. (ii) crescent shaped pores in saddles of folded sheets of clay. E. SE micrograph showing elongated cracks with jagged edges. F. BSE image of E. G. Non-porous quartz grain embedded in the clay matrix, with interparticle pores around the rim of rigid grains. H. BSE image of G. I. Non-porous K-feldspar with no obvious interparticle pores at the boundary between clay matrix and non-porous grain. J. BSE image of I. K. Intraparticle pores in albite and interparticle pores between clay matrix and albite. L. BSE image of J.

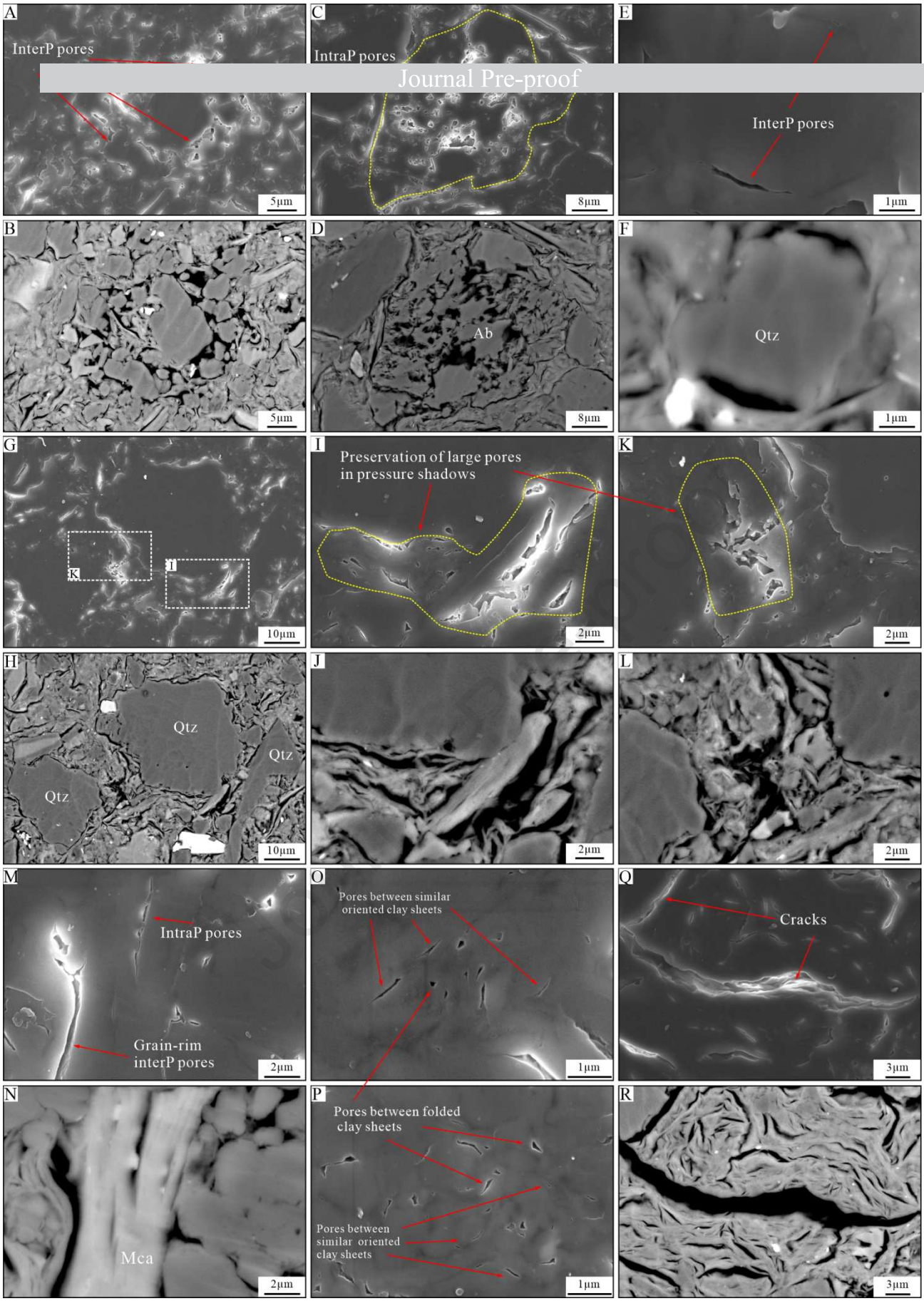

Fig. 4. Sample 2: SE and BSE images of common minerals and associated pores.

A. Interparticle pores within a mixture of rigid grains. B. BSE image of A. C. SE image of albite with large tooth-edged dissolution pores. D. BSE image of C. G. Effect of stress shadowing in silt-rich area, preserving larger pores within the clay matrix. H. BSE image of G. I and K. Enlargement of two parts of the micrograph shown in G, showing the large pores within the less compacted clay matrix. J and L. BSE images of I and K. M. Interparticle pores and pores between detrital sheets of mica. N. BSE image of M. O and P. SE images of pores within the clay matrix. Q. SE image showing an elongated crack in clay matrix and a crack at the rigid particle-clay interface. R. BSE image of Q.

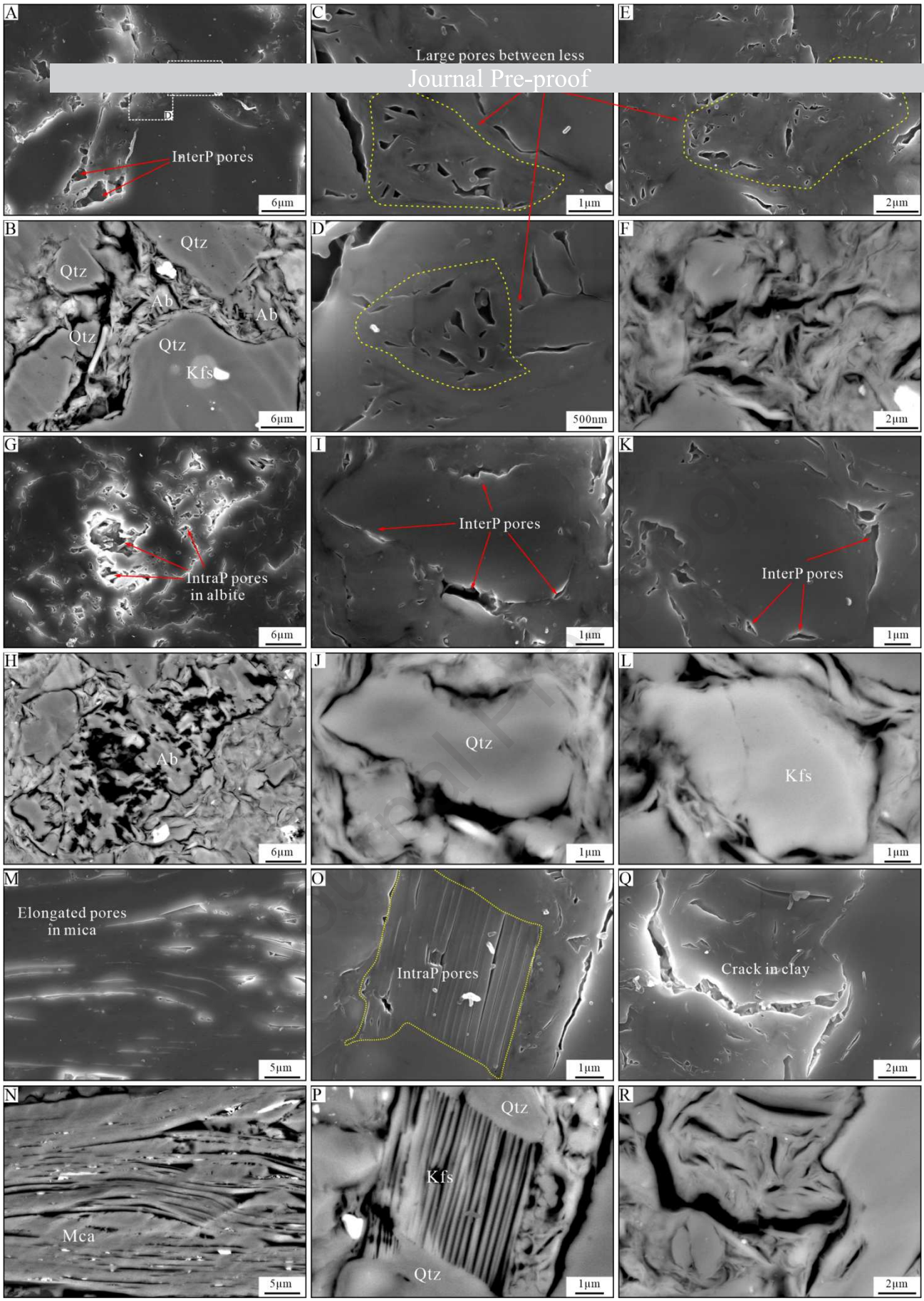

Fig. 5. Sample 3: SE and BSE images of common minerals and associated pores.

A. SE images showing large interparticle pores around rigid grains. B. BSE image of A. C, D, and E. Large pores in the clay matrix as a result of less compaction within grain-supported framework. F. BSE images of E. G. Large dissolution pores in albite. H. BSE image of G. I and K. Interparticle pores at the edges of quartz and K-feldspar grains. J and L. BSE images of I and K. M. Mica with very long, elongated pores between lamellae. N. BSE image of M, indicating some pores in mica are filled with bright minerals. O. Intraparticle pores in K-feldspar, showing morphologies which change from elongated to rounded with increasing degree of dissolution. P. BSE image of O. Q. SE image of the crack in clay. R. BSE image of Q.

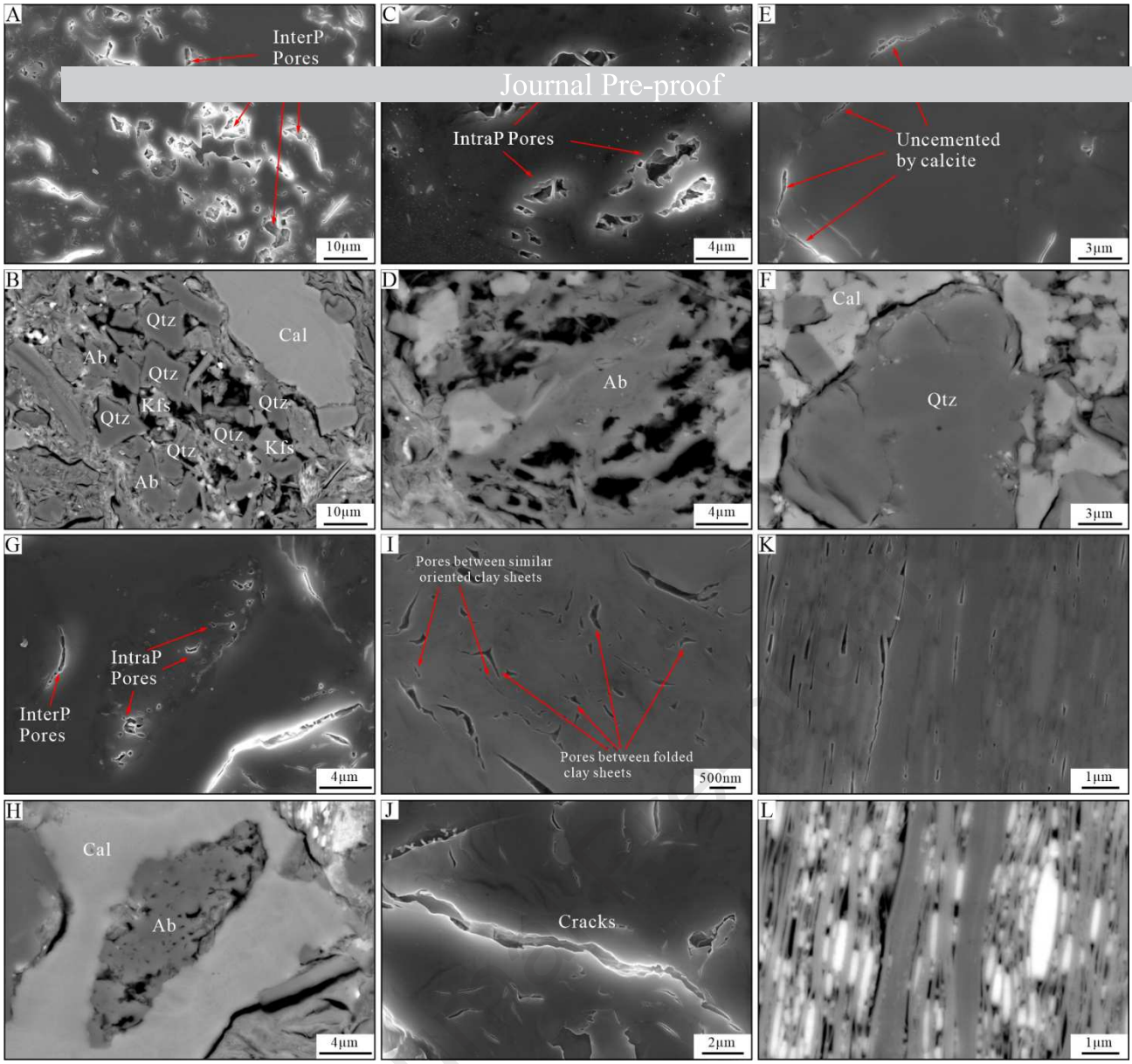

Fig. 6. Sample 4: SE and BSE images of common minerals and associated pores.

A. Large interparticle pores between rigid grains. B. BSE images of A and C. C. Dissolution pores in albite. D. BSE image of E. E. Interparticle pores caused by the incomplete cementation. F. BSE image of E. G. Interparticle pores between calcite crystals and clay, and dissolution pores in albite. H. BSE image of G. I. SE image of pores within clay matrix. J. SE image in a crack within clay matrix. K. Mica with very elongated pores between lamellae. L. BSE image of K.

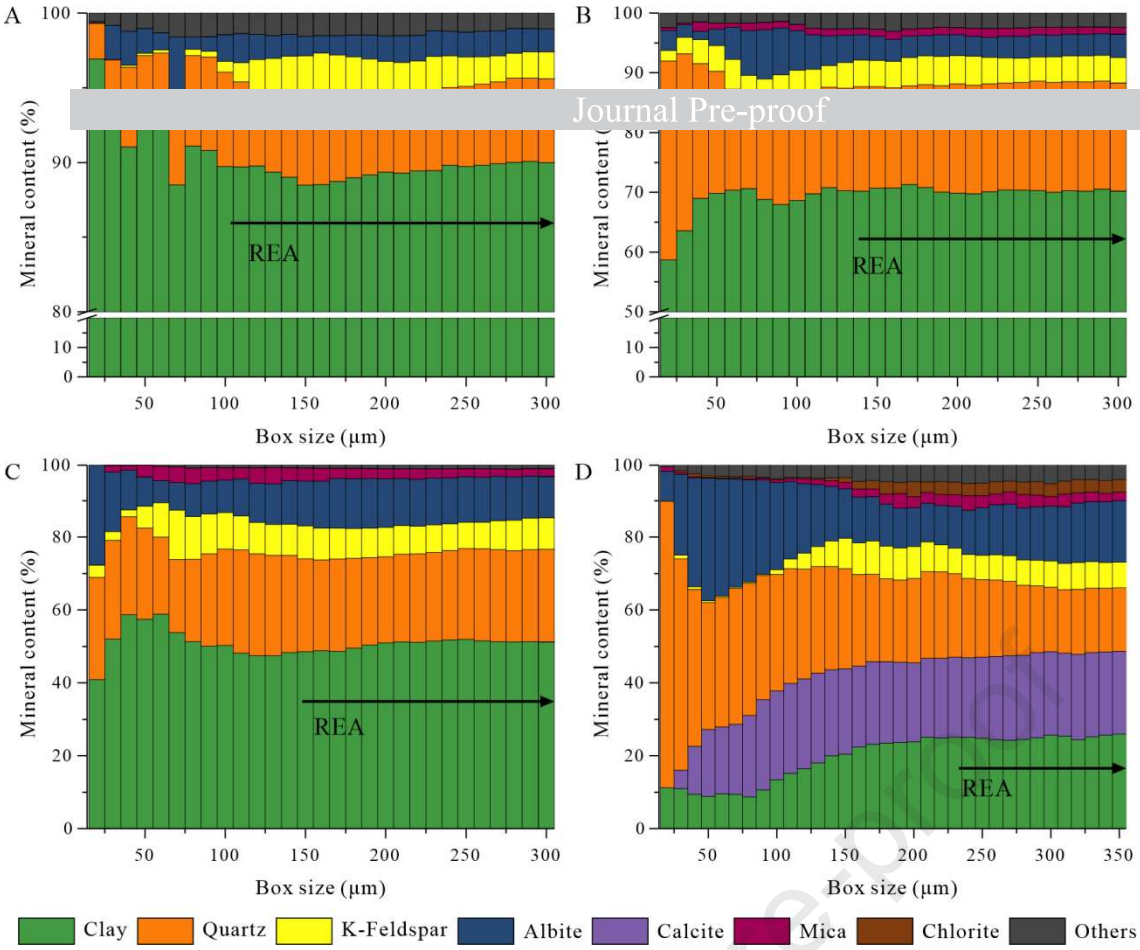

Fig. 7. Representative elementary area (REA) calculations based on mineralogy box-counting method. (A) Sample 1, with a REA of 100 μm × 100 μm; (B) Sample 2, with a REA of 140 μm × 140 μm; (C) Sample 3, with a REA of 160 μm × 160 μm; (D) Sample 4, with a REA of 230 μm × 230 μm

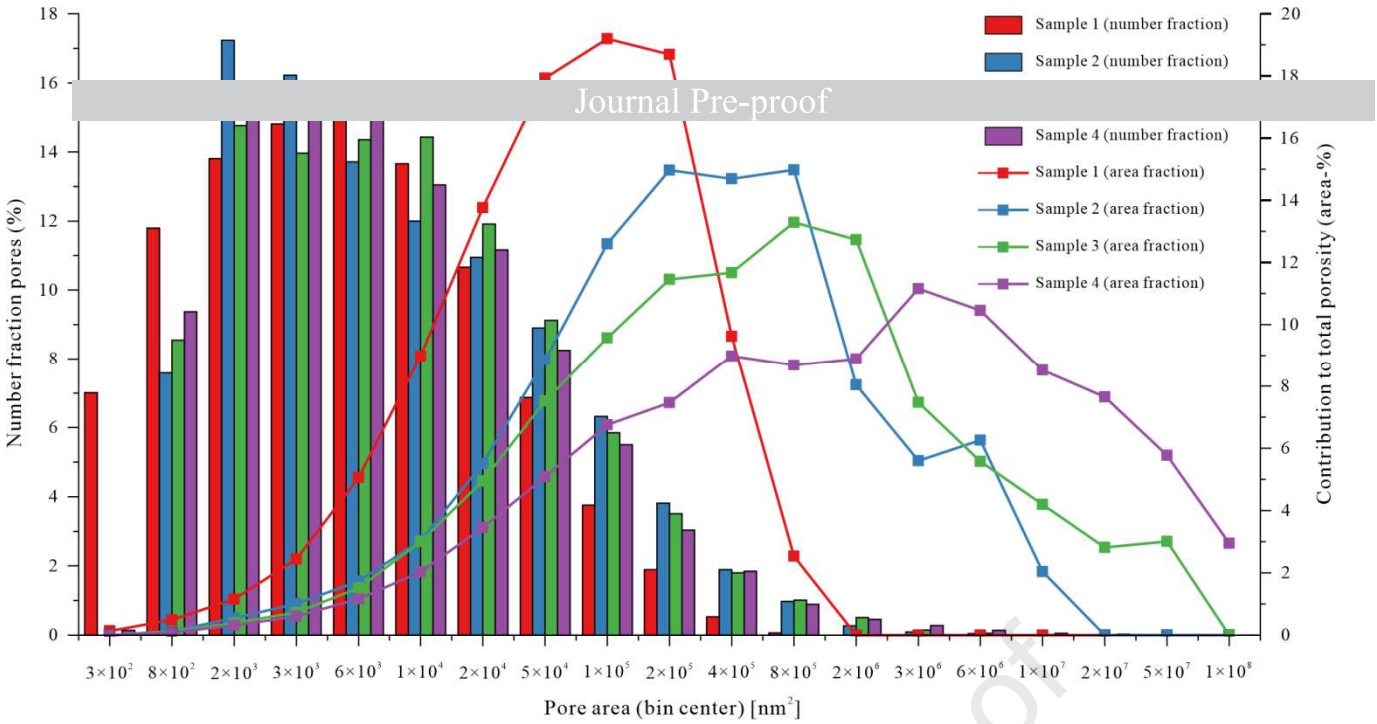

Fig. 8. Number fractions and total porosity contributions of pore-sizes (areas).

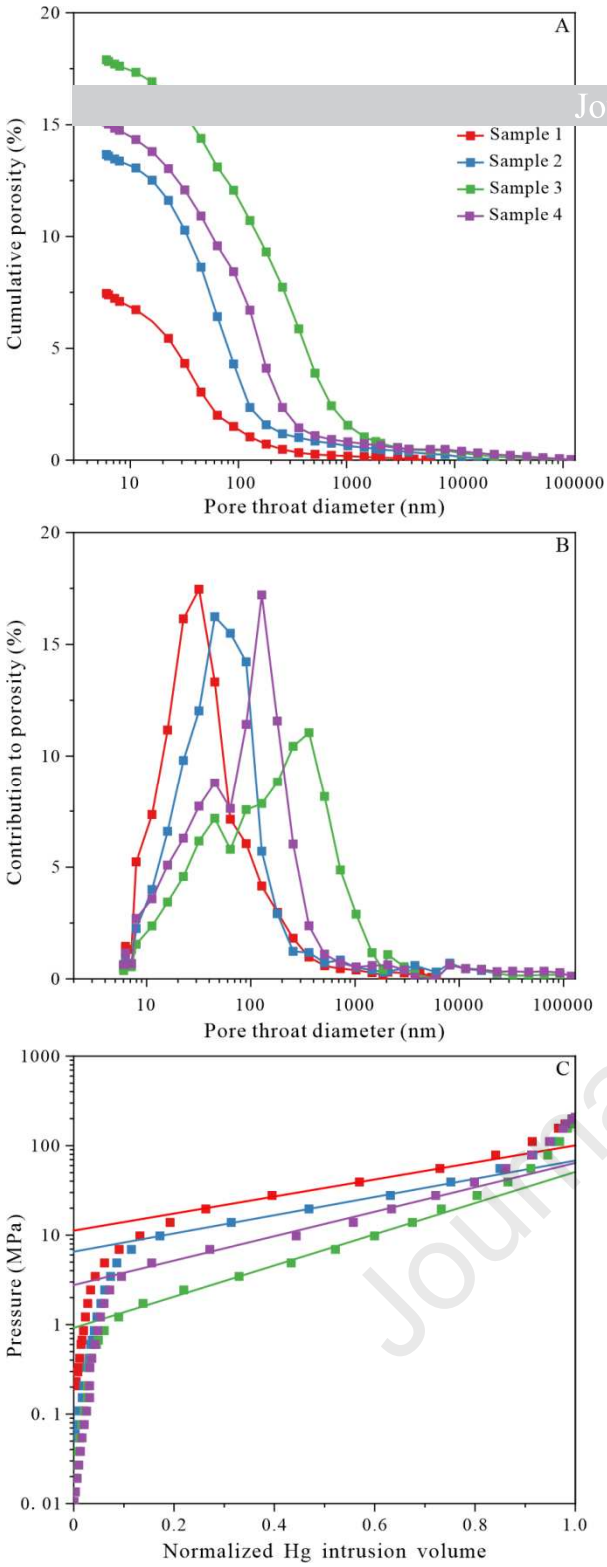

Fig. 9. A. MICP cumulative porosity vs. pore diameter (nm). B. MICP pore size distribution data. C. Estimated capillary breakthrough pressures based on mercury injection porosimetry (tangent to the inflection point of the cumulative intrusion curve and extrapolated to the logarithmic pressure axis).

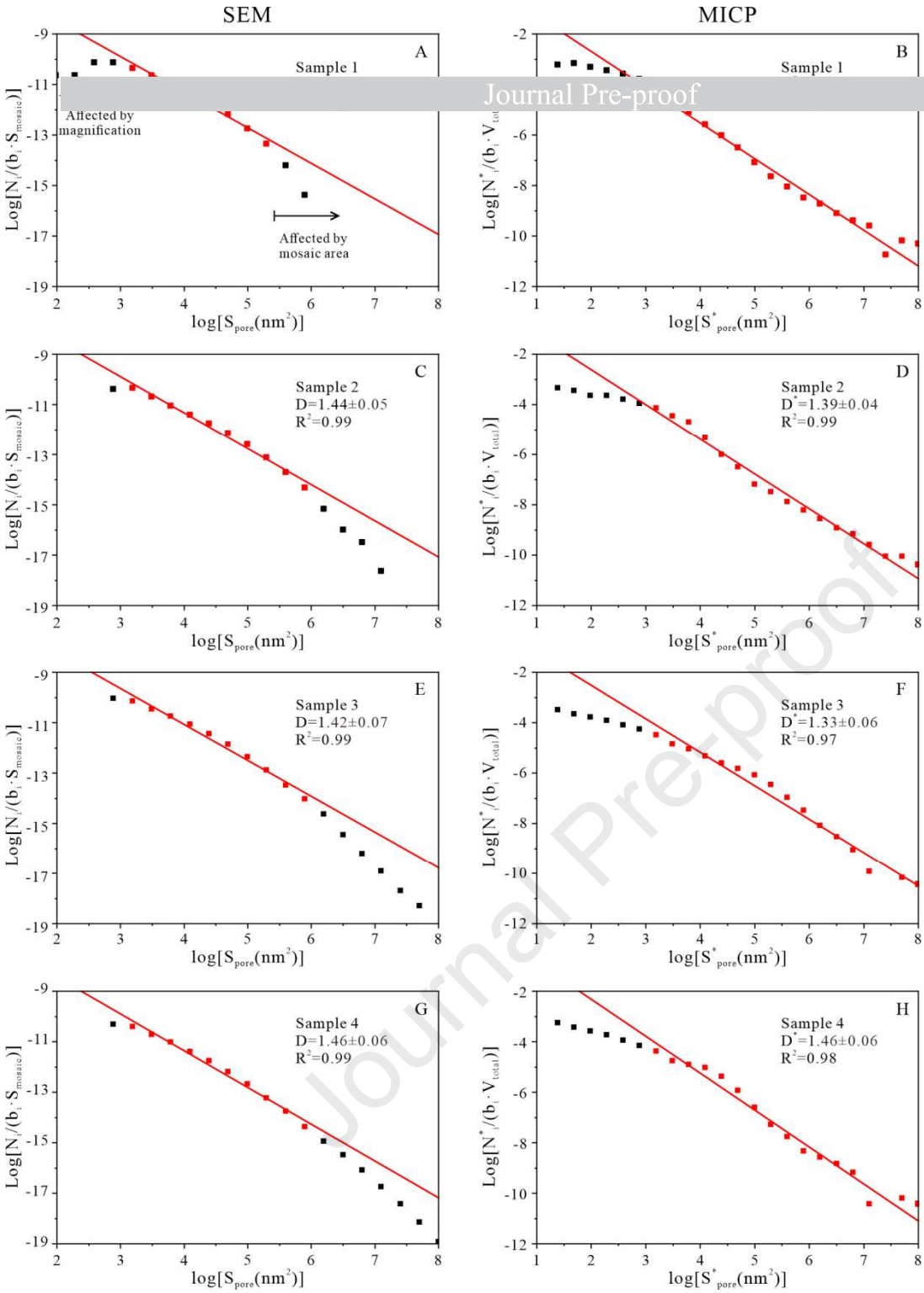

Fig. 10. Pore size distribution inferred from SEM data (A, C, E, G) and MICP data (B, D, F, H). Red, solid line of fit is for the data represented by red squares.

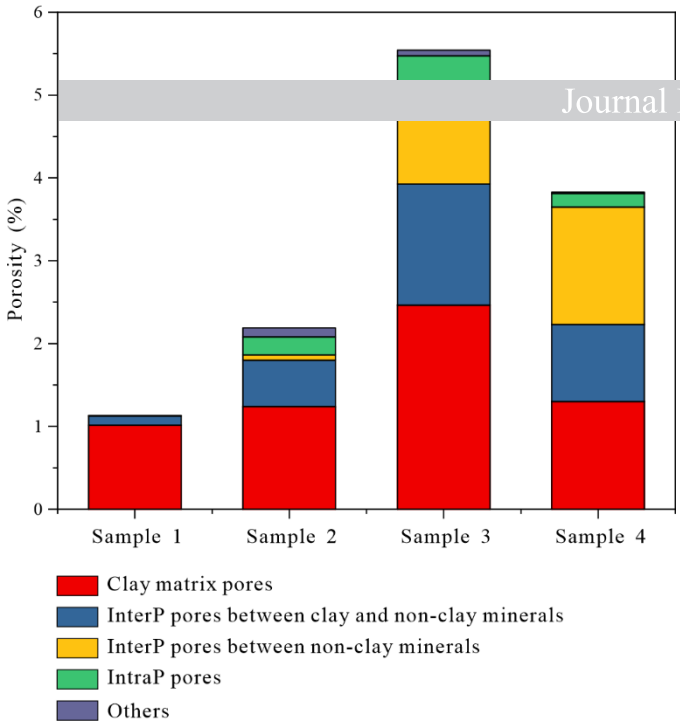

Fig. 11. Porosity and pore classification in each sample.

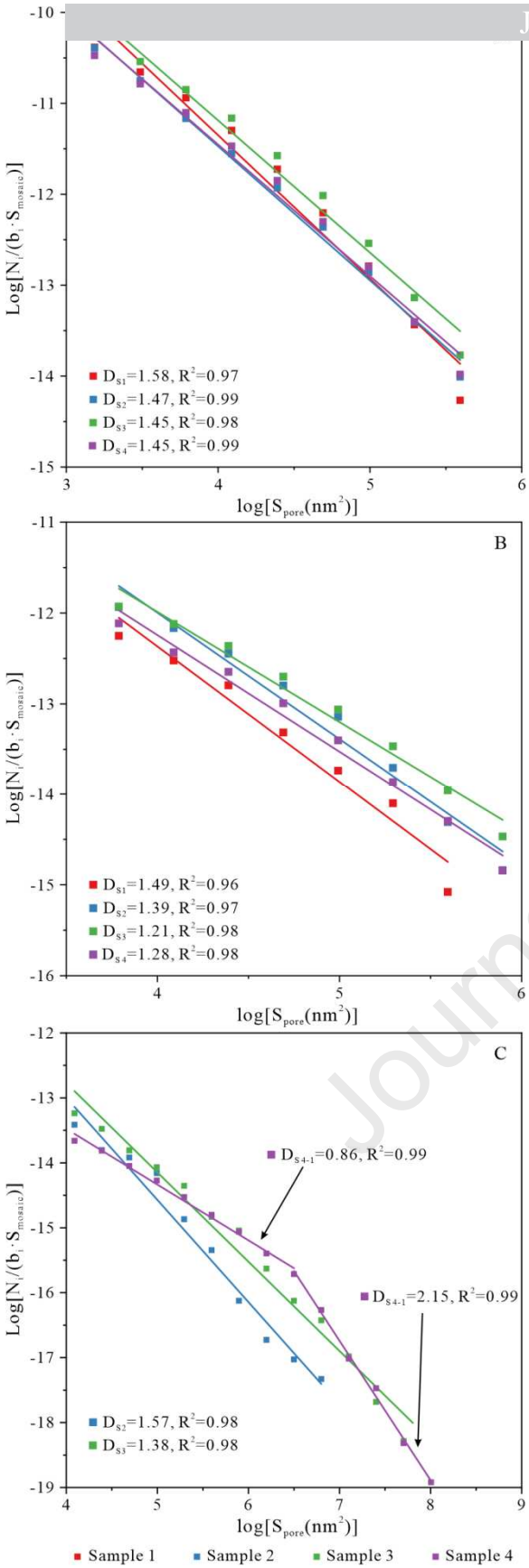

Fig. 12. Normalized size distribution of (A) pores within clay matrix; (B) interparticle pores between clay and non-clay minerals; (C) interparticle pores between non-clay minerals. For each normalized pore size distribution, the best fit is shown as a solid line and the D values are given for each fit.

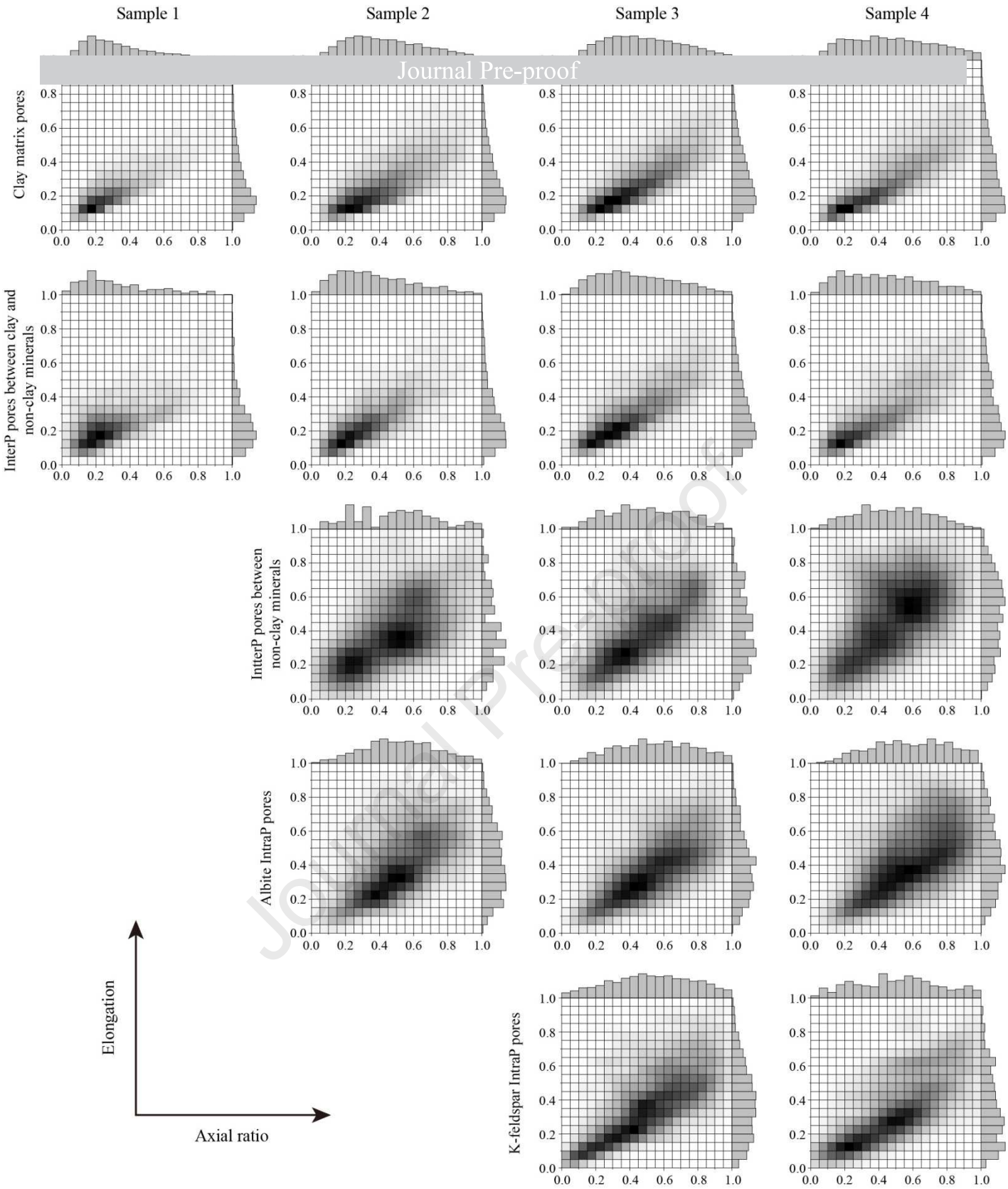

Fig. 13. Data density graphs of the bivariate histograms of the pore shape factors, showing axial ratio (W/L) and circularity of inter and intra pores associated with different minerals.

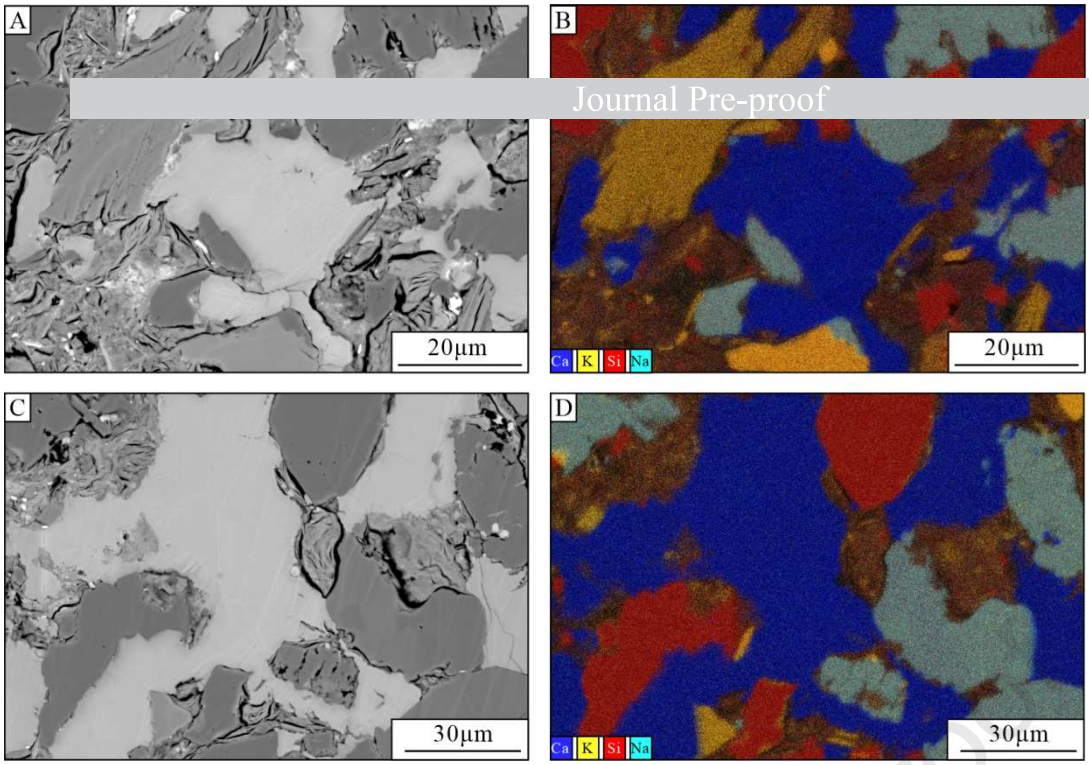

Fig. 14. Calcite cementation in sample 4 as seen in BSE (A and C) and element maps (B and D).

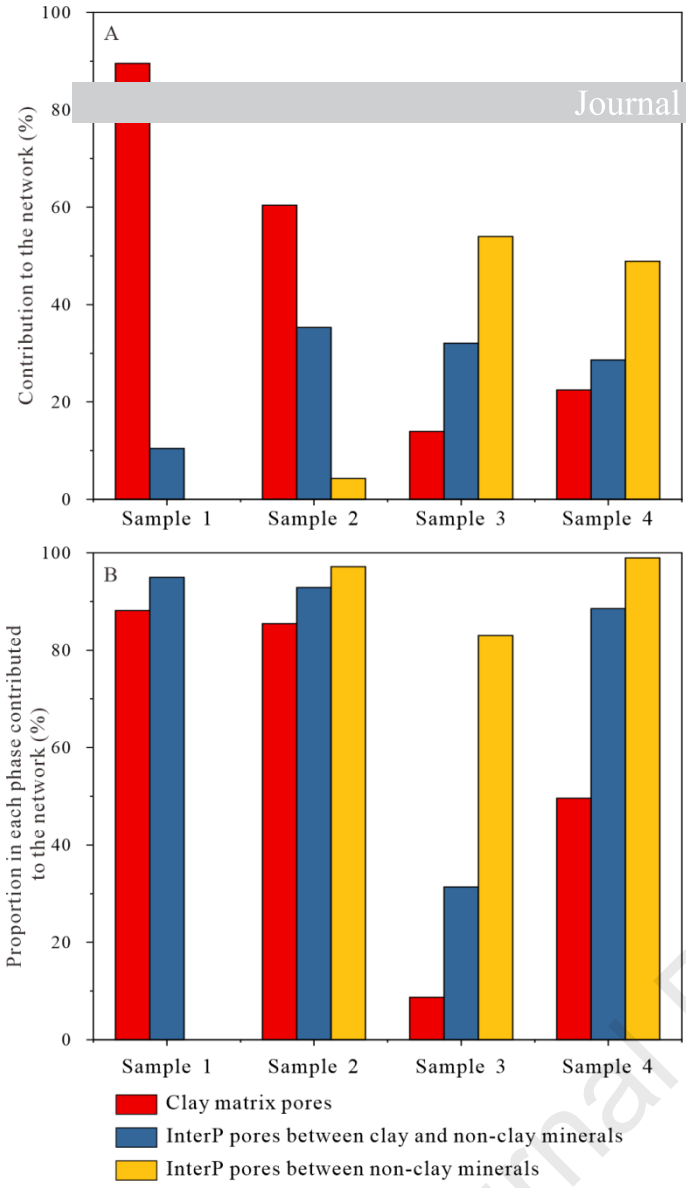

Fig. 15. Contribution to the non-wetting phase-filled pore network (A), and proportion in each phase contributed to the connected network at the critical diameter (B).

Highlights

Pore size distributions and pore morphologies quantitatively analyzed within representative elementary areas.

Pore system controls on capillary breakthrough estimated.

Effect of carbonate cement on pore systems discussed.

Declaration of interests

☒ The authors declare that they have no known competing financial interests or personal relationships that could have appeared to influence the work reported in this paper.

☐The authors declare the following financial interests/personal relationships which may be considered as potential competing interests: